FATIGUE ANALYSIS OF 3D PRINTED 15-5 PH STAINLESS STEEL - A COMBINED NUMERICAL AND EXPERIMENTAL STUDY

A Thesis

Submitted to the Faculty

of

Purdue University

by

Anudeep Padmanabhan

In Partial Fulfillment of the

Requirements for the Degree

of

Master of Science in Mechanical Engineering

August 2019

Purdue University

Indianapolis, Indiana

THE PURDUE UNIVERSITY GRADUATE SCHOOL
STATEMENT OF COMMITTEE APPROVAL

Dr. Jing Zhang, Chair

Department of Mechanical and Energy Engineering

Dr. Andres Tovar

Department of Mechanical and Energy Engineering

Dr. Xiaoliang Wei

Department of Mechanical and Energy Engineering

Approved by:

Dr. Jie Chen

Head of the Graduate Program

To, my wife, the source of my strength
my parents, for their unwavering support
my brother, for his belief in me
my friends, for making my life easier
and to the guiding hand, taking me to my best

ACKNOWLEDGMENTS

I would like to acknowledge the immense support provided to me by Dr. Zhang without who's constant encouragement, I would not have achieved this result. He provided me with unequivocal support to achieve my goals and was patient through my errors. His constant encouragement helped me get the National Science Foundation grant and helped me present papers in several conferences of repute.

I would like to thank Dr. Andres Tovar and Dr. Xiaoliang Wei for their support during my time at the university and for serving as part of my advisory committee.

I would like to thank the support provided by Walmart foundation grant titled, "Optimal Plastic Injection Molding Tooling Design and Production through Advanced Additive Manufacturing", and 3D parts MFG,LLC for 3D printing of the fatigue samples.

I would like to thank my lab mates, Sugrim Sagar, Nishant Hawaldar, Abhilash Gulhane, Xuehui Yang, Lingin Meng among others for all their help and banter.

Last, but not the least, I would like to thank my wife, parents, brother and friends for always standing by my side.

TABLE OF CONTENTS

Page

LIST OF TABLES

LIST OF FIGURES

Figure Page

ABSTRACT

Padmanabhan, Anudeep. M.S.M.E., Purdue University, August 2019. Fatigue Analysis of 3D Printed 15-5 PH Stainless Steel - A Combined Numerical and Experimental Study. Major Professor: Jing Zhang.

Additive manufacturing (AM) or 3D printing has gained significant advancement in recent years. However the potential of 3D printed metals still has not been fully explored. A main reason is the lack of accurate knowledge of the load capacity of 3D printed metals, such as fatigue behavior under cyclic load conditions, which is still poorly understood as compared with the conventional wrought counterpart.

The goal of the thesis is to advance the knowledge of fatigue behavior of 15-5 PH stainless steel manufactured through laser powder bed fusion process. To achieve the goal, a combined numerical and experimental study is carried out. First, using a rotary fatigue testing experiment, the fatigue life of the 15-5 PH stainless steel is measured. The strain life curve shows that the numbers of the reversals to failure increase from 13,403 to 46,760 as the applied strain magnitudes decrease from 0.214% from 0.132%, respectively. The microstructure analysis shows that predominantly brittle fracture is presented on the fractured surface. Second, a finite element model based on cyclic plasticity including the damage model is developed to predict the fatigue life. The model is calibrated with two cases: one is the fatigue life of 3D printed 17-4 stainless steel under constant amplitude strain load using the direct cyclic method, and the other one is the cyclic behavior of Alloy 617 under multi-amplitude strain loads using the static analysis method. Both validation models show a good correlation with the literature experimental data. Finally, after the validation, the finite element model is applied to the 15-5 PH stainless steel. Using the direct cyclic method, the model predicts the fatigue life of 15-5 PH stainless steel under constant

amplitude strain. The extension of the prediction curve matches well with the previously measured experimental results, following the combined Coffin-Manson Basquin Law. Under multi-amplitude strain, the kinematic hardening evolution parameter is incorporated into the model. The model is capable to capture the stresses at varied strain amplitudes. Higher stresses are predicted when strain amplitudes are increased. The model presented in the work can be used to design reliable 3D printed metals under cyclic loading conditions.

1. INTRODUCTION

The field of 3D printing technology is vast, but novel. The widespread acceptance towards the additive manufacturing technology has pushed the pace for standardization of the process. This is necessary to develop engineering confidence in the material and the process. The advantages provided by 3D printing has made it possible for it to be overarching across many fields.

3D printing technology started out as a way to prototype designs for testing. The additive manufacturing process quickly took a more meaningful role as it's benefits were realized. As 3D printing methodology took a mainstream path, there generated a need for understanding and characterizing the various material properties associated with a engineering usage. It's extensive usage in design of engineering components necessitated a need to develop predictive models to determine the material behavior of 3D printed specimen.

1.1 Motivation

Additive manufacturing (AM) or 3D printing process has made rapid strides in recent years. However, the full potential of 3D printing technology hasn't been rigorously explored. There is still a dearth of knowledge about it's mechanical abilities, such as the fatigue behavior under cyclic load conditions. Further still, there is a lack of characterization for a numerical model to predict their mechanical behavior as compared to their wrought counterparts.

There are many methods to assess the fatigue life of structures. Most commonly, one uses the S-N curves for assessing component life. The standard fatigue prediction methods have a linear damage approach. The research conducted in fracture mechanics have established that such an approach is conservative with studies conducted for

the establishment of Paris law [1]. Moreover, there is no information about damage or crack behavior with these approaches. The increasing usage of 3D printed materials in high energy applications has made it critical to have a characterized numerical model which would incorporate non-linearity for damage or crack evolution. To understand the cyclic behavior of 3D printed parts and to characterize the parameters associated with cyclic behavior leading to fatigue would further accelerate acceptance of additive manufacturing process.

1.2 Objective

The goal of the thesis is to advance the knowledge of fatigue behavior of 15-5 PH stainless steel manufactured through laser powder bed fusion process. This is done through a combined numerical and experimental study. First, using a rotary fatigue testing experiment, the fatigue life of the 15-5 PH stainless steel is measured. Second, a finite element model based on cyclic plasticity, including the damage model, is developed to predict the fatigue life. Finally, after model validation, the finite element model is applied to the 15-5 PH stainless steel.

1.3 Structure of the Thesis

This thesis is divided into five sections. The first is the introduction which would cover the motivation, objective and the overall structure of thesis.

The second chapter reviews literature that is relevant to characterization of the cyclic and fatigue properties. It contains an overview of existing works characterizing cyclic 3D printed material properties. Then the concept of fatigue, plasticity and damage mechanics is introduced. These directly relate to material characterization.

The third chapter deals with the experimental procedure that was carried out. The 3D printing process to produce the test specimen and the testing methodology for fatigue are briefly discussed.

The fourth chapter models the cyclic behavior utilizing a finite element tool. The modelling technique employed is discussed. Two calibration simulations are carried out to show model viability and then the said model is applied to develop a predictive model for 3D printed 15-5 PH Stainless steel. The results of the approach are discussed.

The fifth chapter would conclude the findings of this study and the sixth chapter would recommend future work associated with the finite element model.

2. LITERATURE REVIEW

2.1 Additive Manufacturing

Research into the material behavior of 3D printed parts has been going on for decades. Understanding the fatigue behavior of component is critical and to this end, many publications have focused on determining such properties. Sehrt et al. [2] was one of the first to investigate the dynamic properties of 3D printed parts as they determined the fatigue strength of SLM built 17-4 PH stainless steel. They investigated the effect of orientation on the fatigue life. Spierings et al. has conducted numerous investigations [3] [4] [5] to assess the effect of manufacturing parameters on mechanical property, including fatigue life.

Numerical modelling of 3D printed specimen has picked up in the last two years. A similar experiment to the one by Sehrt [2] was conducted more recently by Yadollahi [6] where they characterized the cyclic behavior of 17-4 PH stainless steel with a cyclic Ramberg-Osgood model. They extended this characterization to encompass their dependence on printing orientation. Similar characterization was done for the 3D printed AISI 18Ni30 [7] where the low cycle fatigue characteristics were investigated and fit to Coffin-Manson curve.

2.2 Fatigue, Plasticity and Damage

Throughout history, engineers have worked towards understanding the phenomenon of failure of structures or mechanical parts. It began with the conceptual study of stress and strain and how one could measure failure using these two parameters. Many theories of failure were proposed.

Theories on failure can be broadly classified into macroscopic failures and microscopic failures criteria. The macroscopic criteria usually takes into account the macroscopic effects of stress and strain and include failure theories like von Mises theory, Maximum principal stress theory among others. This approach sticks to the elastic regime and doesn't take into account the toughness of the material after it yields.

The microscopic failure criteria leverages the theories of fracture mechanics and continuum mechanics. These theories are more robust from a theoretical point of view because the mechanism defining failure is explored in detail. They see failures, in this case crack propagation, as irreversible thermodynamic processes and thus can be defined using energy conservation principles.

2.2.1 Fatigue Modelling

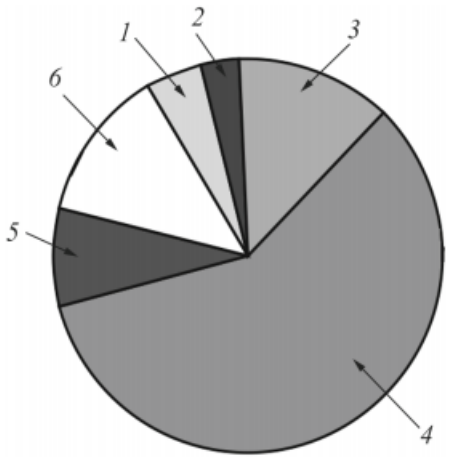

Fig. 2.1. Pie chart representation of causes of structural failure [8]

The term 'Fatigue' was first introduced to mean failure due to repeated cycles of loading, in the middle of 19th century, by J.B.Poncelet [8]. It took the initial works of Wohler, who was an engineer investigating the failure of railroad axles (particularly

the Versailles accident [9] which gave the impetus to this research), to convince the engineers about failures occurring below the monotonic failure limit of the material. This gave rise to $S-N$ curves, also called Wohler curves, that are still used today to predict the fatigue life of material. It was soon to be understood that the primary reason for failure of machine parts was fatigue, see figure 2.1 and table 2.1 [8]. Since then, numerous investigations have been carried out to understand the nature and causes of fatigue failure.

Table 2.1.
Figure 2.1 values [8]

No.	**Failure mode**	**Percent**
1	Delayed corrosion	5%
2	Corrosion cracking	3%
3	Static loading	13%
4	Fatigue	58%
5	Low cycle fatigue	8%
6	Other causes	13%

The stress based methods are more popularly identified as $S-N$ curve methods. This, as discussed earlier, was first introduced by A. Wohler. The fatigue life of a material (cycles N) is related to the cyclic stress range (S) that loads the material. Basquin [10] was the first to recognize the power law based association between the applied stress amplitude and the fatigue life which he captured using the formula,

$$\sigma_a = \frac{E.\Delta\epsilon_e}{2} = \sigma_f^{'}(2N)^b \tag{2.1}$$

where σ_a is the applied stress amplitude, E is the Young's modulus, $2N$ is the load reversals to failure, $\sigma_f^{'}$ is the fatigue strength coefficient, b is the fatigue strength exponent.

Palmgren-Miner introduced the linear cumulative damage hypothesis which applied the S-N curve for variable amplitude loading. This is popularly called the Miner's rule [11] and is given by,

$$\sum_{i=1}^{n} \frac{n_i}{N_i} = 1 \tag{2.2}$$

where, n_i is the number of cycles the material was subjected to at stress σ_i, N_i is the number of reversals to failure at stress level σ_i.

The material is assumed to have failed when the cumulative damage at different stress amplitude σ_i reaches 1. This method was further improved by Goodman, Soderberg and Gerber who introduced the effect of stress ratio and mean stresses on the fatigue life through their respective criteria.

For components subjected to cyclic loads that induce plasticity in the very first cycle, the fatigue life is affected by plastic strains. In this type of loading, it makes more sense for us to define the life of material using the strains as they can be differentiated into plastic and elastic components. This gave rise to strain based fatigue assessments. The relationship, similar to the Basquin relationship, is famously given by Coffin-Manson [12] [13] [14] as,

$$\frac{\epsilon_p}{2} = \epsilon_f^{'}(2N)^c \tag{2.3}$$

where, $\epsilon_p/2$ is the plastic strain amplitude, $\epsilon_f^{'}$ is the fatigue ductility co-efficient and c is the fatigue ductility exponent.

The two models shown by eq.2.1(elastic) and eq.2.3(plastic) are combined and the consolidated total strain to life relationship [14] given as,

$$\frac{\Delta\epsilon_T}{2} = \epsilon_a = \frac{\epsilon_e}{2} + \frac{\epsilon_p}{2} = \frac{\sigma_f^{'}}{E}(2N)^b + \epsilon_f^{'}(2N)^c \tag{2.4}$$

Continuum damage mechanics based approach is a relatively new methodology that posits that strain energy release is the major contributor towards the fatigue failure of materials. This method has been heavily researched beginning with Kachanov

then improved by Chaboche and Lemaitre. This method and fracture mechanics based approaches to fatigue rely on power law based representation of crack propagation.

The continuum mechanics based approach will be discussed in detail in the coming sections. The crack propagation theory is mainly based on Paris law [1] which gives the rate of crack growth as,

$$\frac{da}{dN} = A(\Delta K)^n \ \ where \ \ \Delta K = Y\Delta\sigma\sqrt{\pi a} \tag{2.5}$$

where, A and n are constants for materials and Y is geometry factor depending on mode of loading. K is the stress intensity factor.

The crack propagation was better understood later as having non-linearity. Then three regions describing crack growth was mooted which is seen in fig.2.2.

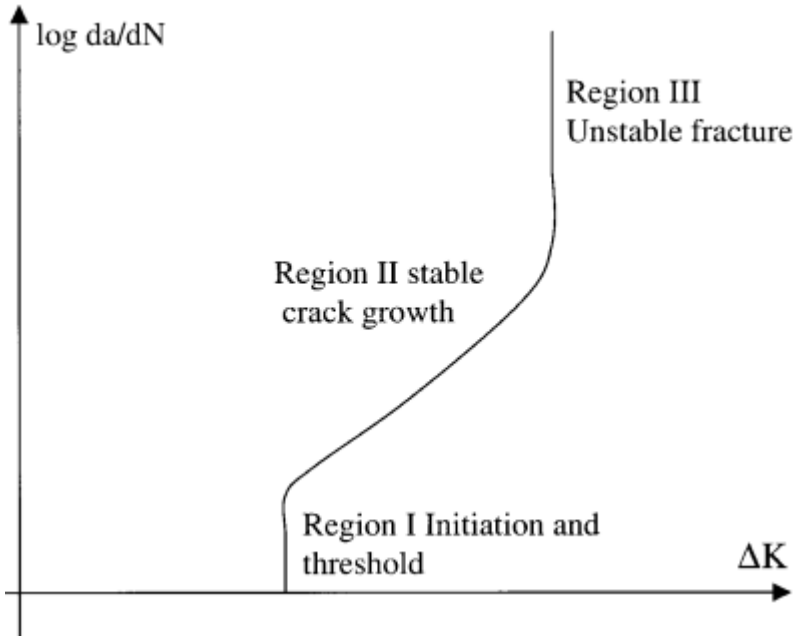

Fig. 2.2. Crack growth rate as a function of K [15]

2.2.2 Modelling Plasticity

Before a ductile material fails, it goes through the process of yielding. This behavior is non-linear such that it is difficult to assign a modulus to predict the loading path. The accurate modelling of this effect is an important tool to understand the evolution of Continuum damage mechanics. This theory primarily relies on the accumulated plastic strains and strain energy density concepts to capture fatigue damage accumulation. A brief summary is provided here.

Elastic deformations are reversible. When a material is loaded beyond it's elastic limit, it undergoes irreversible deformation. On unloading we recover the elastic part of the deformation. The behavior of the material is linear in the elastic zone and becomes non-linear once it crosses the yield point.

As the material crosses yield point, it experiences a coalescence of defects causing a temporary saturation. This makes the material more resistant to deformation and thus can be said to have hardened. This is called strain hardening process.

The total strain of a material would be written as,

$$\epsilon = \epsilon_e + \epsilon_p \tag{2.6}$$

where, ϵ_e is the elastic component and ϵ_p is the plastic component of strain. The stress strain curve is then represented using the Ramberg-Osgood [16] relationship by,

$$\epsilon = (\frac{\sigma}{E}) + (\frac{\sigma}{K})^M \tag{2.7}$$

where, σ is the stress, K and M are material constants. Changes to the Ramberg-Osgood relationship from the viewpoint of damage mechanics would be discussed in section 2.2.3.

The behavior of a material under a single cycle of tension and compression loading and it's evolution through multiple cycles needs to be accurately predicted. The effects of strain hardening on a cycle of tension - compression loading can be explained with the help of Isotropic or Kinematic hardening rules.

In Isotropic hardening, it is assumed that the yield surface of the material would remain the same shape. If a function $F(\sigma_{ij}, K)$ describing the yield surface of a material under hardening effect is written as [17],

$$F(\sigma_{ij}, K_i) = 0 \tag{2.8}$$

where, σ_{ij} is the stress tensor, K_i represents strain hardening parameters, then according to isotropic hardening rule the yield surface changes as such that [17],

$$F(\sigma_{ij}, K_i) = f_0(\sigma_{ij}) - K = 0 \tag{2.9}$$

which shows that the function has changed only by expansion and hasn't changed in shape. The figure 2.3 shows material under a tension-compression loading cycle following the isotropic hardening rule. As seen, the new yield surface is a scaling of the original by kinematic hardening factor. One important implication of this rule is that the yield in tension and compression would be same. This is not true for most materials.

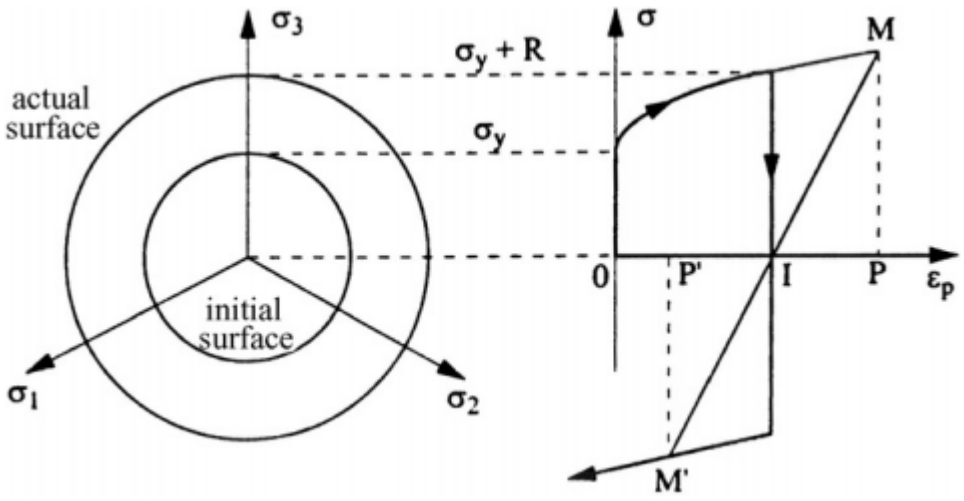

Fig. 2.3. Isotropic hardening surface evolution [18]

Kinematic hardening rule states that the yield surface of the material translates under reversed loading regime. Taking the same yield function, 2.8, the modified yield function for kinematic hardening rule would be [17],

$$F(\sigma_{ij}, K_i) = F(\sigma_{ij} - \alpha_{ij}) = 0 \tag{2.10}$$

where the hardening parameter, α_{ij} is called backstress. Figure 2.4 shows that the

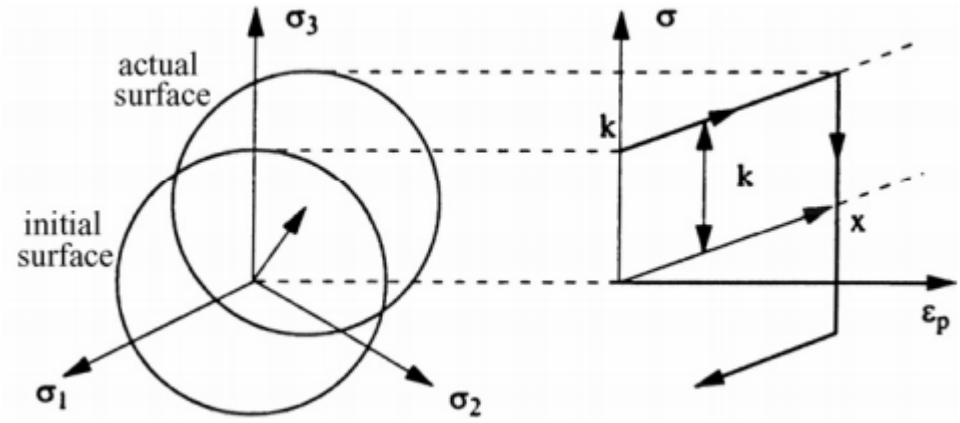

Fig. 2.4. Kinematic hardening yield surface evolution [18]

yield surface has neither changed it's shape or size but has shifted by the hardening parameter(backstress),α_{ij}. The implication of this rule is that the yield point in tension would not be the same as that in compression.

Upon unloading and subsequent compressive loading we see that the yield in compression is less than the yield point in tension. This weakening of material is referred to as Bauschinger effect [19].

In the figure 2.5, O represents the zero stress state, OAB is the loading path the material takes under tension, BC is the unloading stage, CDE is the loading path under compression and EF is the subsequent relaxation. We observe that for most materials, it follows the kinematic hardening path because of which the yield point in tension is less than that in compression($\sigma_{yp} < \sigma'_{yp}$).

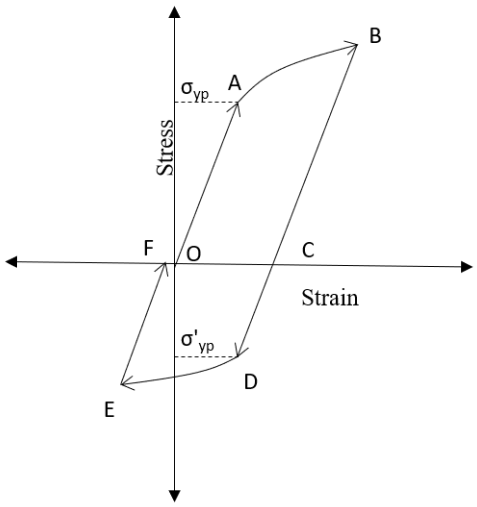

Fig. 2.5. Bauschinger effect [19]

When the material is subjected to cyclic loading, it experiences the hardening effects across multiple cycles as well as within a single cycle. The material can accumulate strains over the span of cycles which essentially means that the cyclic load creates open elasto-plastic loops. Under stress-controlled tests with unsymmetrical loads, we observe that the strains continue to increase cycle by cycle in the direction of unsymmetry.

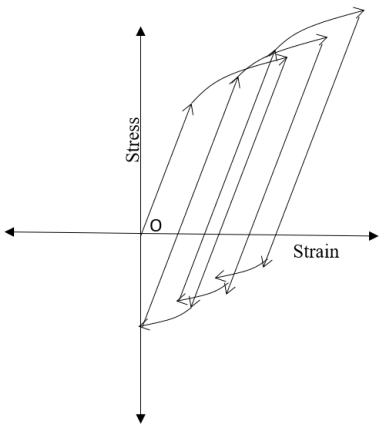

Fig. 2.6. Stress-strain curve with ratcheting phenomenon [18]

The plastic strains keep accumulating and we observe a phenomenon called ratcheting, otherwise known as cyclic creep. This is usually characterized by a shifting hysteresis loop. Fig 2.6 shows the gradual accumulation of strains across multiple loops. The hardening models proposed previously could capture the behavior of single cycle but couldn't predict cyclic phenomenon like cyclic hardening/softening, shakedown or ratcheting. This phenomenon was first categorized by Bree [20] when he tried to explain the thinning of nuclear fuel cans. These components were loaded with pressure internally, were subjected to thermal fluctuations and experienced unsymmetric load cycles. The Bree diagrams were a way for predicting the ratcheting phenomenon. Ratcheting can severely affect the life of components subjected to cyclic loading.

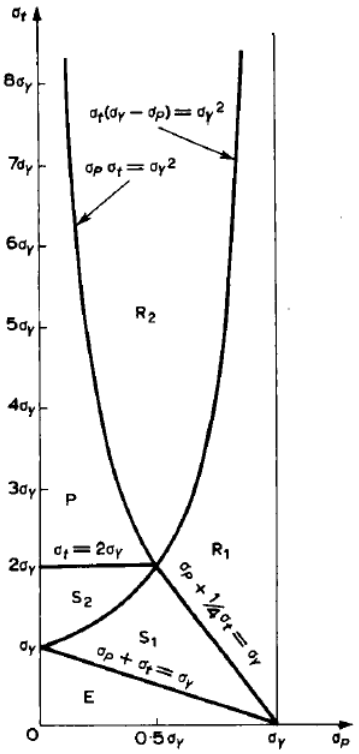

Fig. 2.7. Bree diagram showing stress regimes [20]

Table 2.2.
Stress regime for Bree diagram [20]

Stress regime	**Can behavior**
R_1 and R_2	Ratchetting
S_1 and S_2	Shakedown after first half cycle
P	Plastic cycling
E	Elastic

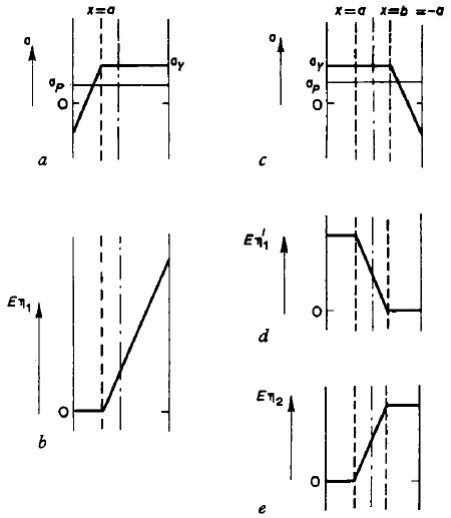

Fig. 2.8. Stress and plastic strain for half cycle of regime $R1$ [20] from figure 2.7

a) Stress incurred by first half of each cycle.

b) Plastic strain incurred by first half-cycle.

c) Stress incurred by second half of each cycle.

d) Plastic strain incurred by second half of each cycle.

e) Plastic strain incurred by first half of each cycle after the first.

The methodologies mentioned above were the first attempts to characterize the cyclic material behavior. The Bree model was considered conservative and efforts to better the model were made. There was a need for a non-linear kinematic/isotropic (combined) hardening (NLKH) model which would be defined as,

$$F(\sigma_{ij}, K_i) = F(\sigma_{ij} - \alpha_{ij}) - K = 0 \tag{2.11}$$

Frederick-Armstrong model [21] is one of the first to predict ratcheting by predicting backstress with,

$$d\alpha = \frac{C}{\sigma_0} dp - \gamma.\alpha.dp \tag{2.12}$$

where, C and γ are material constants to be calibrated and α is the backstress after varying yield limit σ_0 (see equation 2.16) for the plastic strain p. The Chaboche model [18] improved this by generalizing the net as a summation of multiple backstress to capture realistic shapes of stress-strain curve, giving

$$d\alpha = \sum_{i}^{n} \frac{C_i}{\sigma_0} (\sigma - \alpha) dp - \gamma_i.\alpha_i.dp \tag{2.13}$$

It is to be noted that C_i and γ_i are not be considered as material parameters but rather as series decomposition of a simpler expression, for instance, by a power law [18]. The integration of 2.13 would give the monotonic stress-strain curve

$$\sigma(p) = \sigma_0 + \sum_{i}^{n} \frac{C_i}{\gamma_i} (1 - e^{-\gamma_i p}) \tag{2.14}$$

which when further integrated for cyclic stress-strain curve from stabilized cycle gives,

$$\frac{\Delta\sigma(\Delta p)}{2} = \sigma_0 + \sum_{i}^{n} \frac{C_i}{\gamma_i} \tanh \gamma_i \frac{\Delta p}{2} \tag{2.15}$$

where the $\Delta\sigma$ represents the cyclic stress amplitude range for plastic amplitude Δp

With addition of isotropic hardening effect, it is understood that the yield surface in equation 2.15 expands as plastic loading continues. Thus, σ_0 varies as,

$$\begin{aligned} \sigma_0 &= k + R \\ and\ \ R &= Q(1 - e^{-bp}) \end{aligned} \tag{2.16}$$

where k is the initial yield stress of the material during the first half of the first cycle. Q and b are isotropic hardening constants.

The above equation captures the phenomenon of cyclic hardening/softening more accurately. Further, the model could be made sensitive to the variation of γ_i to plastic strain component and have it vary with [22],

$$\gamma_i = \gamma_{i,ini} + \sum_{i=1}^{k} L_i(1 - e^{-d_i p}) \tag{2.17}$$

where $\gamma_{i,ini}$ is the γ value at first cycle. L_i and d_i are kinematic hardening evolution parameters.

2.2.3 Representation of Damage

Damage is a process by which the material loses it's load carrying capacity and ultimately results in breaking of the part. Lemaitre [23] classifies the types of damage variables and their applicability by scale. Damage, at the microscale level, is the concentration of microstresses around defects or interfaces, both of which results in deterioration of material. At the mesoscale level we have to look at the concept of 'Representative Volume Element'(RVE) which is an abstract volume capturing the effects of microscale and translating it into mesoscale without smoothing the high gradients. At this scale, crack is initiated by the coalescing of voids or defects. At the macroscale level, this manifests as growth of crack. The first two stages are modeled using the theory of continua while the third stage is studied using fracture mechanics. We now shall delve into the evolution of this concept.

The first instance of a damage parameter used was in the works of Kachanov [24] to model effects of material deterioration under creep conditions. In his works, Kachanov introduced the concept as the 'continuing parameter',ψ, with

$$0 \leq \psi \leq 1 \tag{2.18}$$

such that $\psi = 1$ represents the condition of undamaged state or virgin material. The material is understood to undergo deterioration as ψ decreases.

Let us consider a damaged material. An RVE is cut out of the bulk with its normal, $\vec{n}$ and let δS be the cross-sectional area of the RVE and δS_{Ds} be the total area of microvoids and cracks on δS. Also defining damage parameter $D(\vec{n}, s)$ with plane s as (see Lemaitre, [23]),

$$D = 1 - \psi \tag{2.19}$$

and

$$D(\vec{n}, s) = \frac{\delta S_{Ds}}{\delta S} \tag{2.20}$$

To get the parameter to be continuous, we take the plane s where the damage is maximum, such that the parameter loses it's dependency on plane,

$$D(\vec{n}) = \frac{\delta S_D}{\delta S} \tag{2.21}$$

A kinetic equation for ψ was developed as,

$$\frac{d\psi}{dt} = F(\psi, \sigma_{ij}, ..), \;\; \psi = 1 \;\; at \;\; t = 0 \tag{2.22}$$

under simplified conditions, $F = F(\frac{\sigma_{max}}{\psi})$, where σ_{max} is the maximum tensile stress at a given point. Kachanov further suggested a power law to represent F.

$$\frac{d\psi}{dt} = -A(\frac{\sigma_{max}}{\psi})^n \tag{2.23}$$

Kachanov's theory didn't couple the phenomenon of creep and damage accumulation. Thus it was modified by Rabotnov [25] by first suggesting additional parameters to capture this effect. This was to be fit by using experimental results. But the main contribution was to directly associate the damage parameter to stresses in material.

Let the RVE be acted upon by a force $\vec{F} = \vec{n}F$, inducing an uniaxial stress

$$\sigma = \frac{\vec{F}}{S} = \frac{\vec{n}F}{S} \tag{2.24}$$

Assuming that no forces are effected by the microvoids and cracks, and that the effective area has been reduced to $S - S_D$, the effective stress, $\tilde{\sigma}$ is given as,

$$\tilde{\sigma} = \frac{\vec{F}}{S - S_D} \tag{2.25}$$

It can also be written as,

$$\tilde{\sigma} = \frac{\vec{F}}{S(1 - \frac{S_D}{S})} \ or \ \tilde{\sigma} = \frac{\sigma}{1 - D} \tag{2.26}$$

where $D = \frac{S_D}{S}$ is the damage variable. Here it is assumed that the behavior of microvoids and/or cracks is same in tension as in compression, which is not the case in practice. Also, material is assumed to be isotropic and the load is considered to be uniaxial. Thus this theory is limited to cases where the compressive loads are small.

Lemaitre [23] proposed that, "The strain behavior of a damaged material is represented by constitutive equations of a virgin material(without any damage) in the potential of which the stress is simply replaced with effective stress". Thus,

$$\epsilon_e = \frac{\tilde{\sigma}}{E} = \frac{\sigma}{(1 - D)E} \tag{2.27}$$

where, ϵ_e is the elastic strain and E is the Young's modulus of the material. Also, the Ramberg-Osgood relation [16] for plastic strain changes to

$$\epsilon = (\frac{\tilde{\sigma}}{E}) + (\frac{\tilde{\sigma}}{K^*})^{M^*} \tag{2.28}$$

where, ϵ is the total strain, K^* and M^* are material constants.

Assuming small deformation loads, the total strain can be split into two parts, a thermo-elastic part ϵ^e and a plastic part ϵ^p, giving

$$\epsilon_{ij} = \epsilon^e_{ij} + \epsilon^p_{ij} \tag{2.29}$$

The Helmholtz specific free energy is a function of parameters affecting the stress-strain curve, including damage. Let us consider this measure with $\psi(\epsilon_{ij}, D, etc.,)$. It can be argued that this too would have a distinct elastic and plastic components. It is more convenient to use the Gibb's specific free enthalpy(ψ^*) here such that [23],

$$\psi^* = \psi_e^* + \frac{1}{\rho}\sigma_{ij}\epsilon_{ij}^p - \psi_p - \psi_T, \tag{2.30}$$

where, the thermal component ψ_T is not considered further in this work, and $\psi_p = \frac{1}{\rho}(\int_0^r R dr + \frac{1}{3}C\alpha_{ij}\alpha_{ij})$ is the contribution from plastic hardening. Multiplied by density ρ it is energy stored w_s in the RVE. Another important point is to observe that the term ψ_e^* ensures coupling between elasticity and damage through effective stress concept discussed earlier.

The state laws derived from this formalism are,

$$\begin{aligned} \epsilon_{ij} &= \rho\frac{\partial\psi^*}{\partial\sigma_{ij}} \\ R &= -\rho\frac{\partial\psi^*}{\partial r}, \\ X_{ij} &= -\rho\frac{\partial\psi^*}{\partial\alpha_{ij}} \\ Y &= -\rho\frac{\partial\psi^*}{\partial D} \end{aligned} \tag{2.31}$$

The kinetic laws for evolution of these internal variables are derived from a dissipation potential (F) which is written as [23],

$$F = F(\sigma, R, X_{ij}, Y; Detc.,) \tag{2.32}$$

This potential can be split into components like plastic criterion (f), non-linear kinematic hardening term (F_X) and damage potential (F_D). The evolution laws are written as the contributing component derivative with a time dependent variable.

$$\begin{aligned} \dot{\epsilon_{ij}^p} &= \dot{\lambda}\frac{\partial F}{\partial\sigma_{ij}} \\ \dot{r} &= -\dot{\lambda}\frac{\partial F}{\partial R} \\ \dot{\alpha_{ij}} &= -\dot{\lambda}\frac{\partial F}{\partial X_{ij}} \\ \dot{D} &= \dot{\lambda}\frac{\partial F}{\partial Y} \end{aligned} \tag{2.33}$$

The components of evolution laws are incorporated along with the principle of strain equivalence, and the thermo-elastic law thus derived from the strain potential is,

$$\epsilon_{ij}^{e} = \frac{1+\nu}{E}\tilde{\sigma_{ij}} - \frac{\nu}{E}\tilde{\sigma_{kk}}\delta_{ij} \tag{2.34}$$

where the effective stress is $\tilde{\sigma_{ij}} = \frac{\sigma ij}{1-D}$. The energy density release rate, associated with damage can be written as,

$$Y = \frac{\tilde{\sigma_{eq}^2}R_\nu}{2E} \tag{2.35}$$

and the triaxiality function,

$$R_\nu = \frac{2}{3}(1+\nu) + 3(1-2\nu)(\frac{{\sigma_H}^2}{\sigma_{eq}}) \tag{2.36}$$

where $\sigma_H = \sigma_{kk}/3$ is the hydrostatic stress, $\sigma_{eq} = \sqrt{\frac{3}{2}\sigma_{ij}^D\sigma_{ij}^D}$ the von Mises equivalent stress. The derivations are curtailed for the sake of brevity, a detailed discussion could be obtained from Lemaitre's book [23].

Damage Initiation

The materials exhibit a certain resistance for damage initiation during plastic loading or fatigue. There is a threshold associated with stored energy (w_D) required for the defects to coalesce. From the different hardening and elasto-plasticity laws we can define stored energy as [23],

$$w_s = \int_0^t (R\dot{r} + X_{ij}\dot{\alpha_{ij}})dt \tag{2.37}$$

Consider the associated plastic strain p_s and threshold plastic strain p_D. It is shown that the isotropic hardening saturates at the value $R = R_\infty$ for large p and we know that $p = r$ for $D = 0$ and also recall the state laws from which we have $X_{ij} = 2/3C\alpha_{ij}$ giving us,

$$w_S \approx R_\infty p + \frac{3}{4C}X_{ij}X_{ij} \quad \text{as long as D} = 0 \tag{2.38}$$

The values for parameters X and R depend heavily on the type of hardening laws that are used. An accurate way to describe the phenomenon would be to write,

$$\max w_s = w_D \quad \text{at damage initiation} \tag{2.39}$$

Monotonic tension experiment give the corresponding plastic threshold (ϵ_{pD}) and the fatigue tests would give the accumulated plastic strain (p_D) for a plastic loading range ($\Delta\epsilon_p$) (see figure 2.9).

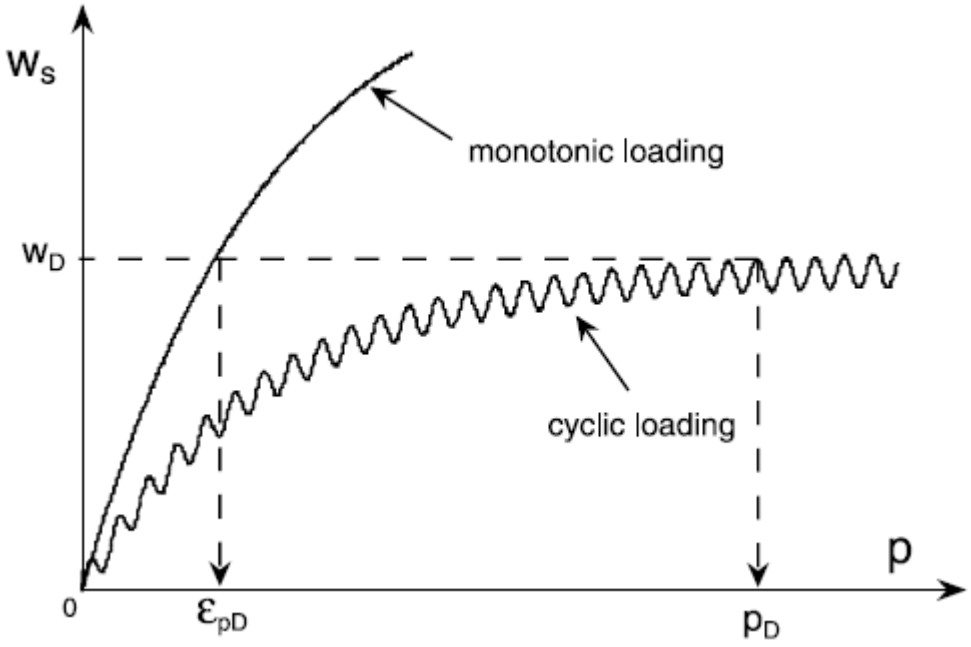

Fig. 2.9. Monotonic and cyclic plastic strain threshold [23]

Damage Evolution

Once the damage is initiated, the material softens considerably and we notice a gradual descent in the maximum stress response. The material loses it's ability for plastic work and the plastic dissipation tends to zero as damage increases and finally, asymptotically, reaches the value of 1. The yield surface of the material would have reached the highest stress for that cycle and the material would have lost all it's plastic ability.

2.2.4 Implementation of the Constitutive Model in FE Tool

There are many commercial FEA tools that enable us to model damage for monotonic load cases. In the current research a commercial software that has incorporated the damage model for cyclic loading with the help of direct cyclic algorithm (see section 2.3), is used.

The step-wise procedure is as follows,

- Step 1: Get the cyclic stress-strain graph from stabilized cycles. Fit the curve so that we obtain the parameters for combined hardening model.Use the parameter for material input. These are critical to assess the hysteresis energy for damage models.
- Step 2: Obtain cycles to damage initiation from cyclic stress-strain data and calibrate it for the damage model.
- Step 3: Obtain fatigue life through experiment and calibrate the total life for the damage evolution.
- Step 4: Use the model to predict fatigue life of material.

Many finite element tools support the combined hardening model and this could be obtained under the plasticity section. To use the damage capability for fatigue, the damage inititation and evolution critieria is defined using the hysteresis energy option. In this existing finite element tool, this is achieved by adding the following lines to the input file,

*Damage Initiation, criterion=HYSTERESIS ENERGY

Data1,Data2

*Damage Evolution, type=HYSTERESIS ENERGY

Data1,Data2

In the finite element tools, the damage initiation criteria is defined as the point where the hysteresis energy reaches a certain threshold value leveraging the thermo-

dynamic theory. It assigns a cycles to initiation value that needs to be calibrated (see [23] section 1.3 for more detail). The equation that finite element tools solves is,

$$N_0 = C_1 \Delta W^{C_2} \tag{2.40}$$

where C_1 and C_2 are material properties that need to be calibrated. When number of cycles $N > N_0$, damage is initiated.

Once the damage is initiated, the material softens considerably and we notice a gradual descent in the maximum stress response. The material loses it's ability for plastic work and the plastic dissipation tends to zero as damage increases and finally asymptotically reaches it's maximum value. The yield surface of the material would have reached the highest stress for that cycle and the material would have lost all it's plastic ability.

The rate of loss of inelastic hysteresis energy is modelled to predict the fatigue life of the material. Finite element tools have an established methodology for fatigue where the damage would tend towards the value of 1 as the inelastic hysteresis energy would tend towards zero and is given by,

$$\frac{dD}{dN} = \frac{C_3}{L_e} \Delta W^{C_4} \tag{2.41}$$

where, C_3 and C_4 are material properties that need to be calibrated, L_e is the characteristic length of the element. The characteristic length and it's effects would be discussed in the section 2.3.3.

Once this cycle number is reached, the damage manifests as macroscopic crack and thus we would define that as the fatigue life for the material.

2.2.5 Procedure for Determination of Material Parameters

Cyclic Hardening Parameters

As seen in the previous section, for us to assess the fatigue life of material through energy methods, the inelastic hysteresis energy should be accurately modelled. And for that, the stress-strain curve should be captured in detail for cyclic loading. We are using the combined hardening model, see eq.2.15, with four backstresses to simulate the cyclic behavior. Now, the kinematic hardening parameters are derived from the stress-strain data by the method of power law regression analysis [26]. Ideally, the values of C_i and γ_i should be calibrated using both monotonic and cyclic data from stabilized cycle.

The extraction of parameter is done through a optimization procedure through MS Excel. A seed value of parameters C_i and γ_i is considered and then the value of $\sigma(p)$ is calculated using the equation 2.14. The difference in the calculated value (from the seed values of C_i and γ_i) to the actual value through experiment (error) is squared and added.

The objective is thus to minimize this error. Excel offers multiple tools to conduct optimization studies. For our purposes we used the GRG non-linear solver with the central difference method. The parameters thus calibrated are seen in Chapter 4.

Let the vector $\vec{W}$ be the calculated values from seed values and let $\vec{V}$ be the actual value from the experiments, then objective function would be,

$$minimize \sum_{i=1}^{n} (W_i - V_i)(W_i - V_i) \tag{2.42}$$

Damage Initiation Parameters

The cycles to damage initiation requires us to carefully plot the cyclic variation of stress-strain hysteresis loops and observe when the angle of linear region (i.e, elastic region) changes. We have defined damage such that $\tilde{E} = E/(1 - D)$ and thus we

see a deterioration in the value of Young's modulus, E, when damage is non-zero. Loading the specimen cyclically between different strain ranges would give different stable inelastic energy values and different cycle life. A plot of different inelastic hysteresis energy values against cycles to damage initiation is created and a power law regression is used to fit the model to the equation $N_0 = C_1 \Delta W^{C_2}$.

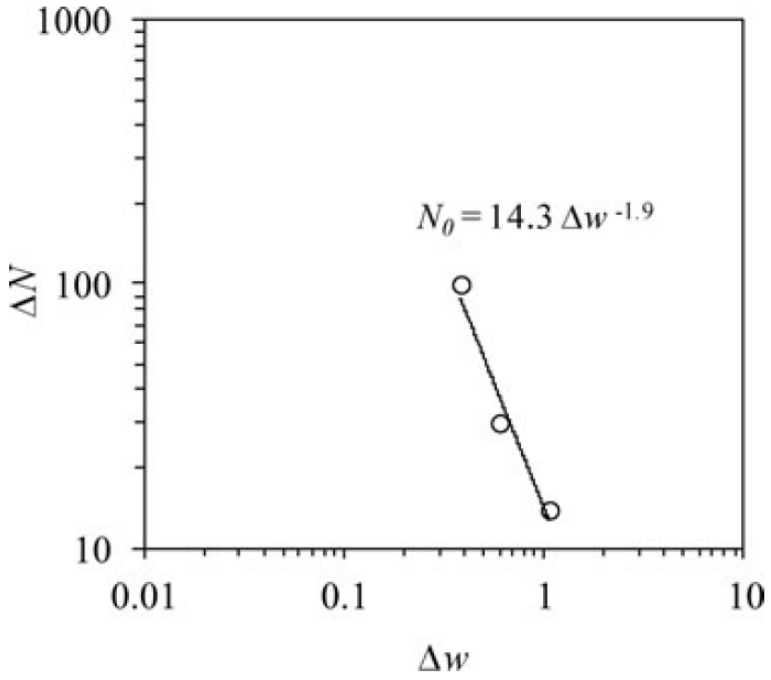

Fig. 2.10. Calculating damage initiation parameters C_1 and C_2 from hysteresis energy [27]

Biglari et al. [27], conducted fatigue inspection for 9Cr steel at $620°C$. They calibrated the damage initiation parameters by tabulating the variation of hysteresis energy with cycles to damage initiation. The data is represented in figure 2.10. They calibrated the initiation parameters to be $C_1 = 14.3$ and $C_2 = -1.9$.

Damage Evolution Parameters

The evolution of material degradation is calibrated by fitting the model for change in inelastic hysteresis energy at different cycles. The experimental data is used to

calibrate dD/dN incrementally. Biglari et al. [27] conducted this calibration for 9Cr steel at $620°C$ using figure 2.11. He obtained the value of $C3 = 4X10^{-}4$ and $C_4 = 0.91$. The value of C_3 is calibrated keeping the characteristic length of mesh used.

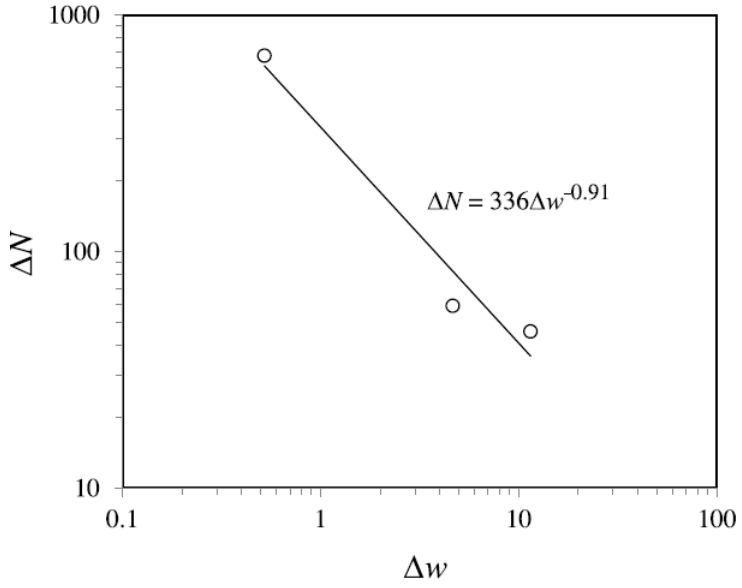

Fig. 2.11. Calculating damage evolution parameters C_3 and C_4 [27]

2.3 Direct Cyclic Method

2.3.1 Need for a Quasi-static Approach

There are various ways to calculate the fatigue life of a component. The most popular way is to conduct a static analysis on the component and after looking up the regions of stress and it's distribution, compare the values to a standard Stress-life curve. These charts provide the life of a component against a given stress value. For low cycle fatigue, a similar strain-life curve is used to assess the life of the material more popularly. The strain measure is accurate for low cycle fatigue regimes. Another way is to refer the Coffin Manson laws to predict the life for both HCF and LCF. These

too would require static analysis result and assume that the rate of crack propagation is linear. Also, we intended to capture the effect of damage through cycles.

To achieve that would be computationally prohibitive. The fatigue analysis involves repeated cycles of static loading and to run those many static cycles is inefficient. Even to predict the stable hysteresis loop for a material subjected to reversed plastic strain cycles would require considerable computation time.

Direct methods for finding stabilized material response were explored for the very same reason. The methodology incorporated in commercial finite element tools is based on the seminal works of Dang and Maitournam [28] who leveraged the cyclic behavior to find Fourier series expansion. The overall methodology is shown in figure 2.12.

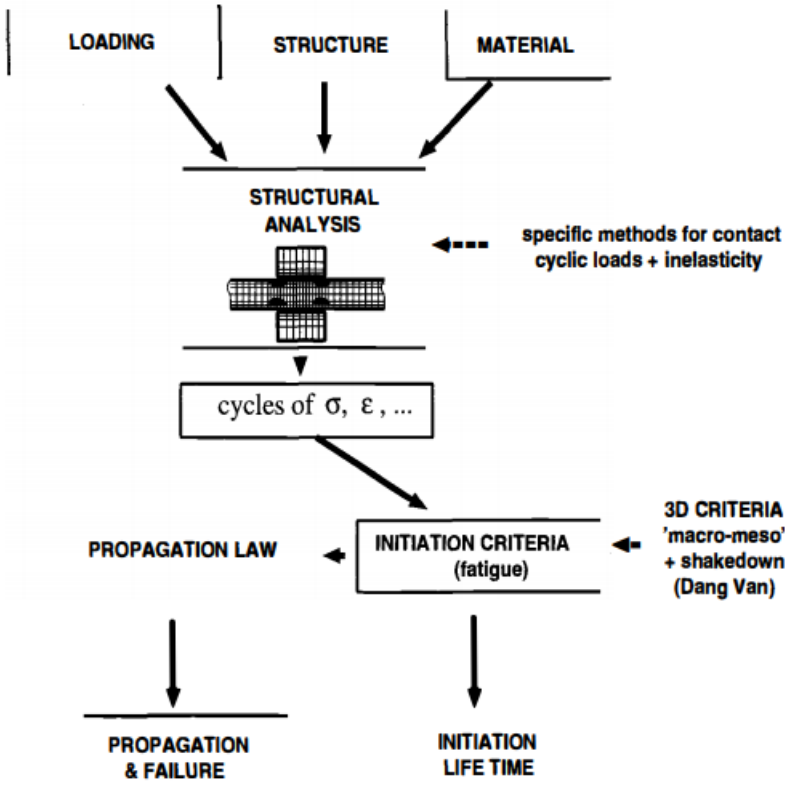

Fig. 2.12. Methodology incorporated by Dang et al. [28]

The stable cycles which are predicted by the hardening laws are reached by enforcing the deformation and force ranges to acquire cyclic values consistent with values at the stabilized cycle. This method predicts the asymptotic material response directly without actually calculating through all cycles. The method works on large time incrementation method and seeks the mechanical fields which have the same values at the end of a loading cycle as the beginning of the cycle. This method can predict elastic and plastic shakedown as well as ratchetting [28].

2.3.2 Implementation in FE Model

We can incorporate direct cyclic algorithm using user defined subroutines. Few commercial finite element tools incorporate the direct cyclic algorithm for both arriving at the aymptotic response as well as predicting the fatigue life. The program solves the familiar equilibrium equation using Newton's method, but the equilibrium equations are now cyclic in nature such that,

$$R(t) = F(t) - I(t) = 0 \tag{2.43}$$

where, $F(t)$ is the descretized form of cyclic load such that $F(t+T) = F(t)$ with time period T, $I(t)$ is the internal force vector and $R(t)$ is the residual vector.

As discussed earlier, we need a displacement definition that is uqual to the values at asymptotic cycle state and thus [29],

$$u(t) = u_0 + \sum_{k=1}^{n} [u_k^s \sin k\omega t + u_k^c \cos k\omega t \tag{2.44}$$

where n is the number of Fourier terms used, ω is the angular frequency, and u_0, u_k^s, u_k^c are unknown displacement co-efficients. The equilibrium equations representing the process are then written as,

$$K c_k^{i+1} = R_k^i \tag{2.45}$$

where, k is the elastic stiffness matrix and i is the iteration number. The residual vector is similarly expanded as the displacement function [29],

$$\bar{R}(t) = R_0 \sum_{k=1}^{n} [R_k^s \sin k\omega t + R_k^c \cos k\omega t] \tag{2.46}$$

where the R_0, R_k^s, R_k^c are found by the fourier term expansion.

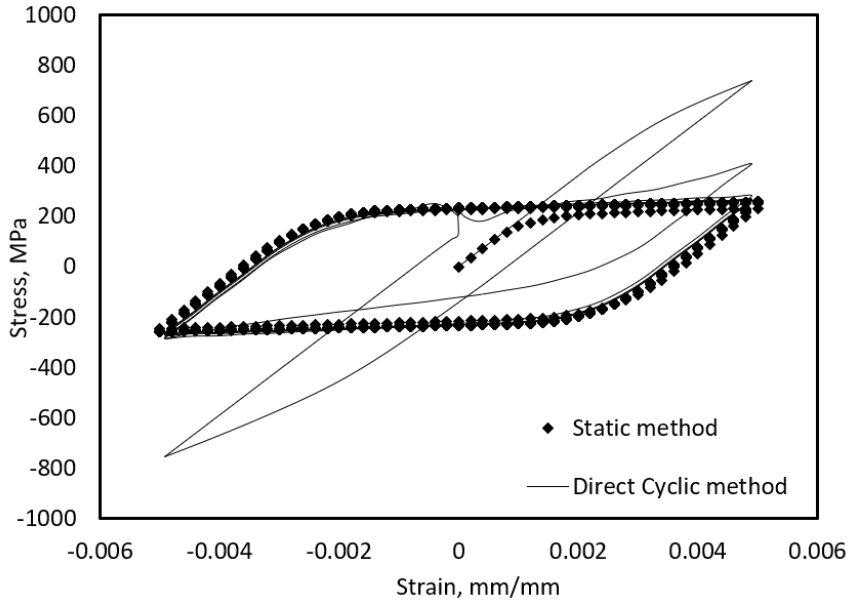

Fig. 2.13. Comparison of stabilized cycle obtained by direct method with static cycling method

The difference between the input and response is fed back as corrections to find the stabilized cycle. The figure 2.13 shows the stabilized state achieved with direct cyclic algorithm with the material loaded cycle by cycle. The computation time saved was significant.

2.3.3 Solution Accuracy

The implementation of fatigue analysis with direct cyclic method needs hysteresis energy for damage calculations. But it is to be noted that the hysteresis energy is sensitive to mesh parameter with it reaches large values as mesh size decreases [30].

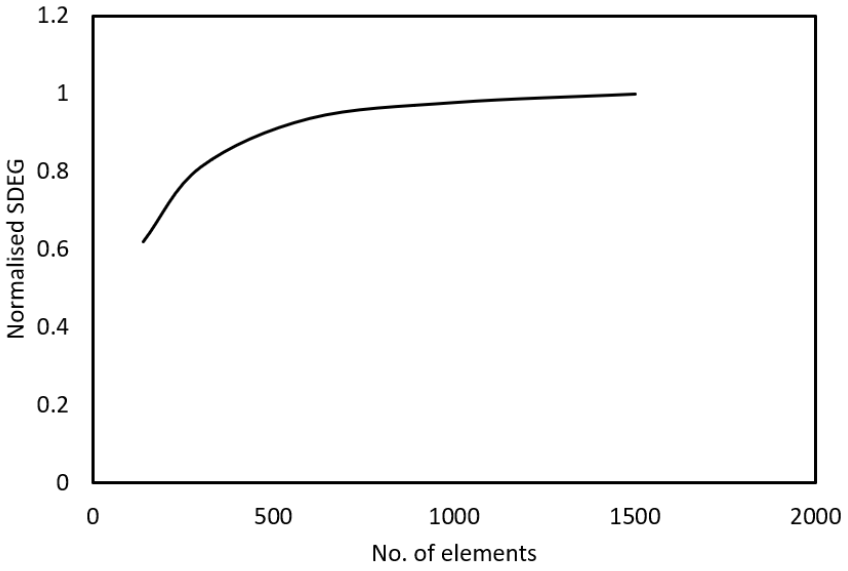

Fig. 2.14. Convergence study for damage parameter

To alleviate this issue, characteristic length is introduced in the damage evolution equation 2.41. According to reference [31],

> The characteristic length is based on the element geometry and formulation: it is a typical length of a line across an element for a first-order element; it is half of the same typical length for a second-order element. For beams and trusses it is a characteristic length along the element axis. For membranes and shells it is a characteristic length in the reference surface. For axisymmetric elements it is a characteristic length in the rz plane only. For cohesive elements it is equal to the constitutive thickness. This definition of the characteristic length is used because the direction in which fracture occurs is not known in advance. Therefore, elements with large aspect ratios will have rather different behavior depending on the direction in which the damage occurs: some mesh sensitivity remains because of this effect, and elements that are as close to square as possible

are recommended. However, since the damage evolution law is energy based, mesh dependency of the results may be alleviated [31].

Therefore, a mesh convergence study targeting the characteristic length has to be conducted as shown in figure 2.14. The characteristic lengths used in this report are 0.266 for the axisymmetric element and 1.58 for the solid brick element.

3. EXPERIMENTAL PROCEDURE

3.1 Preparation of Specimen

The 3D printed specimen is printed using a powder bed fusion process using EOS 270 M. The powder is obtained from EOS who specialise in manufacturing metal powder for 3D printing application. The PH1 series of steels are pre-alloyed steels characterized by good corrosion resistance and excellent mechanical properties [32]. The chemical composition is as shown in table 3.1,

Table 3.1.
Chemical composition of 3D printed 15-5 PH stainless steel [32].

Element	% **by Weight**
Carbon	0.07
Manganese	1.00
Silicon	1.00
Chromium	14.00-15.50
Nickel	3.50-5.50
Copper	2.50-4.50
Molybdenum	0.50
Niobium	0.15-0.45
Iron	Balance

The figure 3.1 shows the SEM image of the powder used to print the specimen for the fatigue test. The average size of the particle can be seen as around 20 μm.

The printed specimen, see figure 3.2 is as per the specification for the the fatigue tester by TERCO for their fatigue testing machine MT3120 [33]. Originally the

specimen was printed with support structures which need to be machined off before using them in the fatigue tester. This was achieved by initially using hack saw blade to remove a considerable portion of support before using a grinding machine to give an accurate finish.

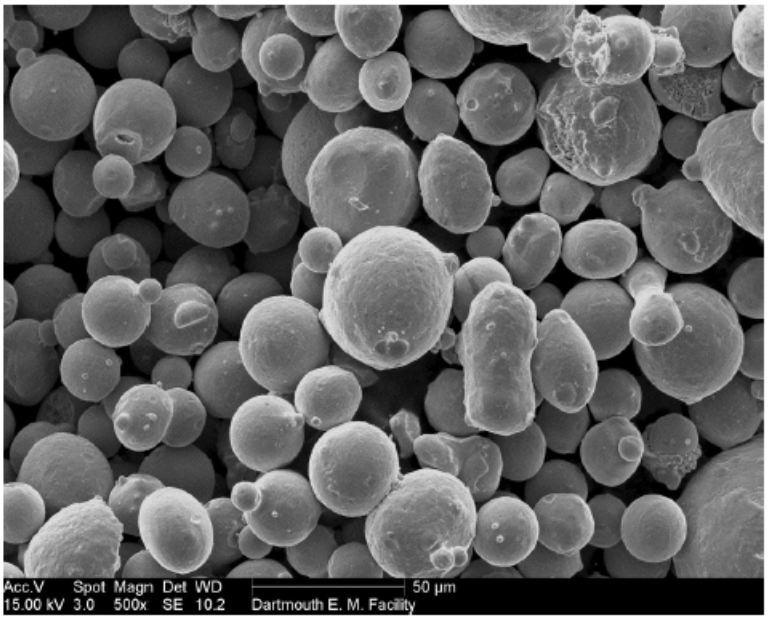

Fig. 3.1. SEM image of 15-5 PH powder [34]

Fig. 3.2. 15-5 PH rotating bending specimen

3.2 Fatigue Testing of Specimen

The fatigue testing machine used was MT3120 fatigue tester from TERCO sweden. The working principle for the machine is as shown in figure 3.3. The actual tester is shown in figure 3.4.

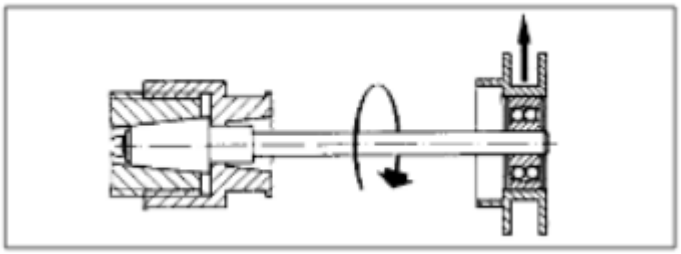

Fig. 3.3. Functioning of MT3120 [33]

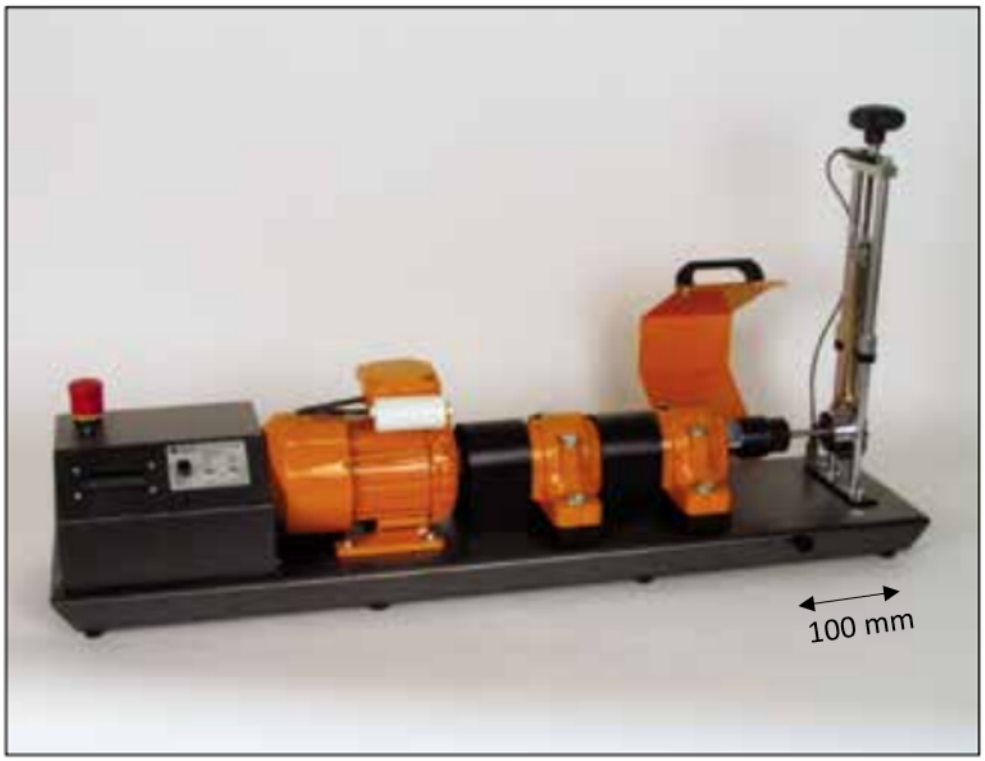

Fig. 3.4. MT3210 Fatigue tester [33]

The specimen showed previously is loaded at the free end in the fatigue tester. The tester has a digital cycle counting device that keeps track of the loading cycles and it automatically stops on specimen failure. The 3D printed specimen were loaded for 3 different strain ranges and the cycles to failure was noted.

3.3 Results and Discussion

The results of the fatigue test is tabulated below,

Table 3.2.
Fatigue result tabulation

% strain amplitude ϵ_a	**No. of reversals to failure**
0.132	46760
0.189	33183
0.214	13403

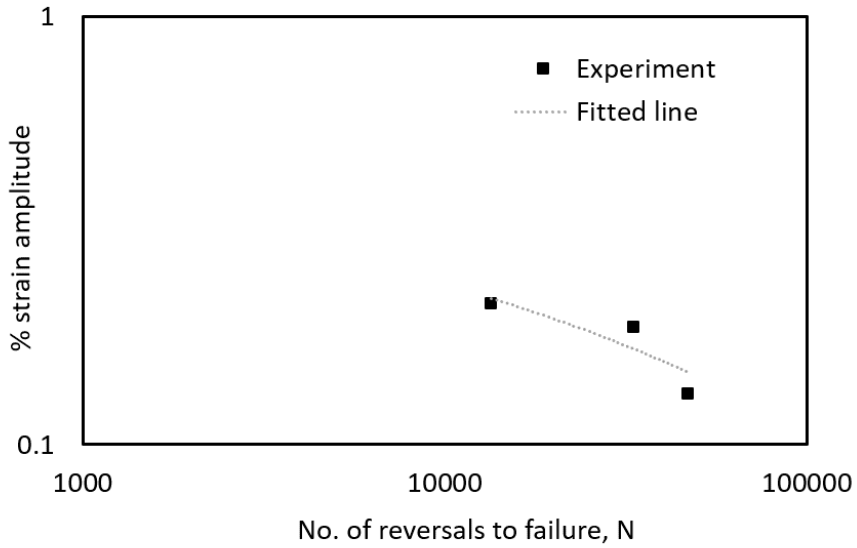

Fig. 3.5. Result of the fatigue test

Fig. 3.6. The specimen after fatigue failure

The strain-life graph, shown in figure 3.5 shows that for higher strain amplitude the specimen takes less number of reversals to failure. The overall trend is that the fatigue life increases with decreasing strain load.

The broken samples are shown in figures 3.7(a) and 3.7(b). In these we can see that the fracture originated at the surface of the specimen. The serrations beginning at the surface and moving inwards are indicative of crack coalescence. This is followed by relatively smooth transition which could be indicative of rapid growth of crack.

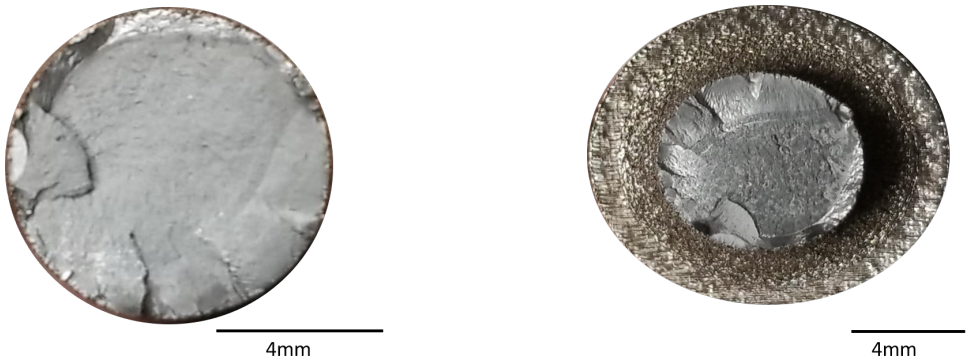

(a) Specimen fracture surface A (b) Specimen fracture surface B

Fig. 3.7. Complimentary specimen surfaces after fatigue failure

4. NUMERICAL MODELLING

Two calibration tests have been simulated using finite element method to demonstrate viability of the model. This is followed by two prediction simulations for 15-5 PH stainless steel. In these simulations, the fatigue prediction is made utilising the direct cyclic algorithm and the cyclic behavior during multiple amplitude strain loading is simulated using the static analysis method. This is because, as mentioned in the section 2.3, the direct cyclic method converges only to the asymptotic stress-strain cycle and thus wouldn't capture the intermediate effect of cyclic hardening or softening. To see how the material behaves through cycles, initially static analysis method is considered.

4.1 Model Validation

4.1.1 CASE 1: Fatigue Prediction for 3D Printed 17-4 Stainless Steel under Constant Amplitude Strain Load: Direct Cyclic Method

The test is to accurately capture the fatigue life of 3D printed 17-4 stainless steel as mentioned in Yadollahi et al. [6]. This specimen was vertically printed. The paper provides the cyclic stress-strain variation and fatigue life at different strain amplitudes. Using these data, the non-linear kinematic hardening parameters, damage initiation and damage evolution parameters were independently calibrated.

Geometry, Mesh and Boundary Condition

The geometry is that of a standard tension compression fatigue test specimen.

The specimen is modelled using axisymmetric elements with 1700 elements and 1806 nodes. The associated characteristic length is 0.266. The element type is ca-

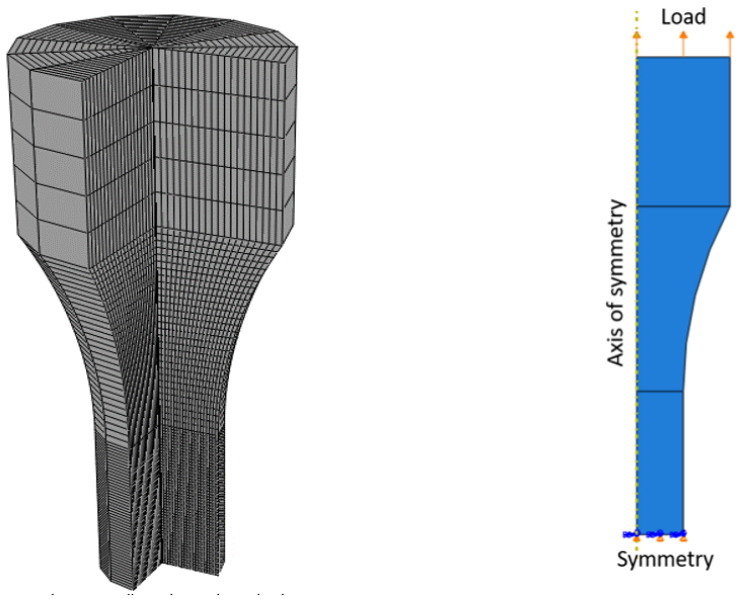

(a) Mesh (b) Boundary condition

Fig. 4.1. FE model for axial Tension-compression fatigue test specimen

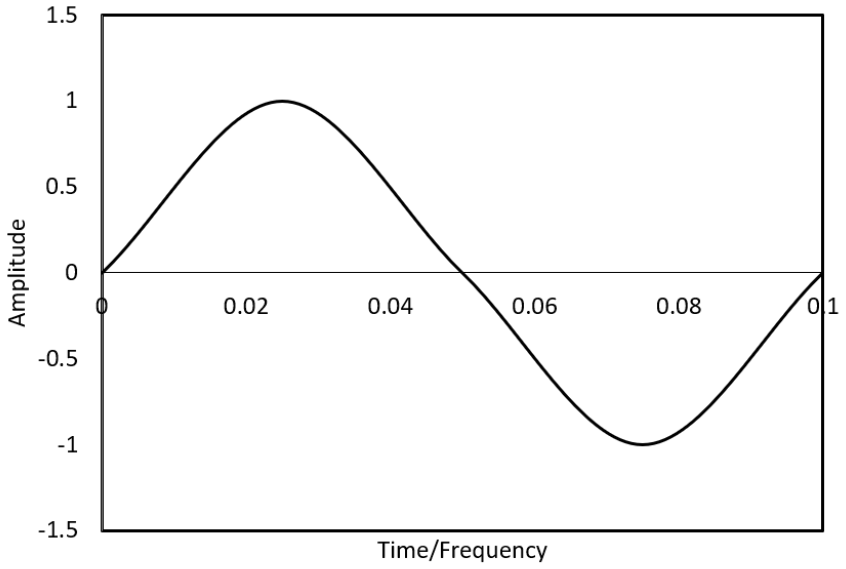

Fig. 4.2. Load function

pable of modelling non-linear plasticity. The model was also symmetrical about the plane perpendicular to it's long axis as shown in figure 4.1. This was done to save computational time and effort.

The specimen was loaded cyclically at top using a cyclic displacement function. The tests were conducted for three strain ranges all multiplied by the amplitude of the displacement function. The three strain ranges were 0.3%, 0.4%, and 0.5%.

Material Parameters

The Young's modulus of the vertically printed, as-built 17-4 PH stainless steel is 187.3 GPa and it's yield strength is given as 580 MPa. The cyclic material parameters were curve fitted using the data given in Yadollahi et al. [6] for the vertically printed, as built specimen. Their cyclic hardening model obtained from stabilized cycle was modified to accommodate the combined hardening model with three backstresses using equation 2.15.

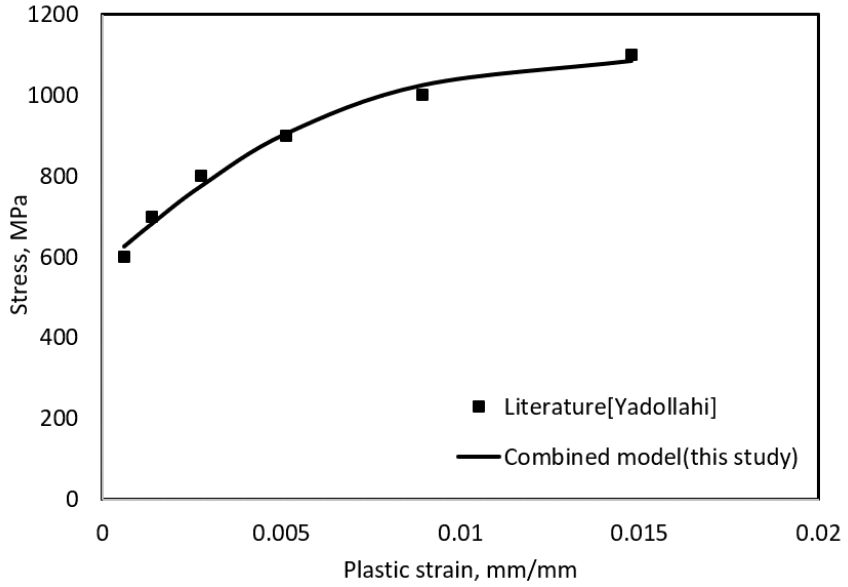

Fig. 4.3. Material characterization for 17-4 [6]

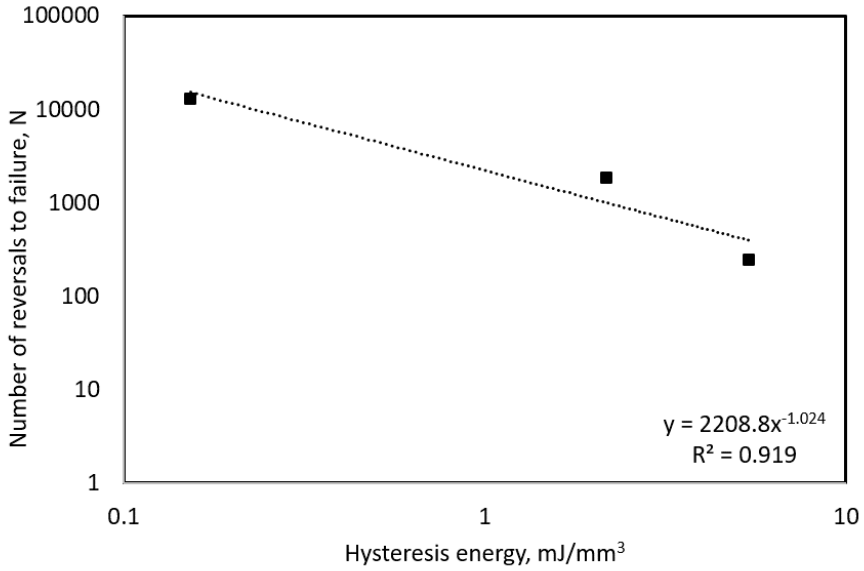

Fig. 4.4. Regression fit for damage evolution

Table 4.1.
Backstresses C_i and γ_i values for 3D printed 17-4 stainless steel

Backstresses	C_i **(MPa)**	γ_i
1	1.83e+5	104516
2	7.145e+4	676060.6
3	7.39e+4	142.59

Table 4.2.
Damage parameters for 3D printed 17-4 stainless steel

Damage parameters	**Values**
C_1	14.3 [27]
C_2	-0.91 [27]
C_3	1e-4
C_4	1.024

The damage parameters were calibrated based on the fatigue life at defined strain amplitudes per Yadollahi [6]. The data provided cannot be used to calibrate damage initiation parameter and thus a nominal value obtained from Bilgari et al. [27] is used in this simulation. The damage evolution parameters are fit for three different strain ranges giving three different hysteresis energy curves, see figure 4.4.

Since our characteristic length is 0.266, we will get the damage evolution parameters as shown in table 4.2.

4.1.2 CASE 2: Cyclic Behavior Simulation for Alloy 617 under Multi-amplitude Strain Load: Static Analysis Method

Pritchard [35] conducted experiments detailing the behavior of steel Alloy 617. The focus of his work was to establish fatigue life and fatigue-creep life of the alloy and explored strain rate dependence of material parameters. An attempt has been made to replicate the the multi-amplitude strain range behavior.

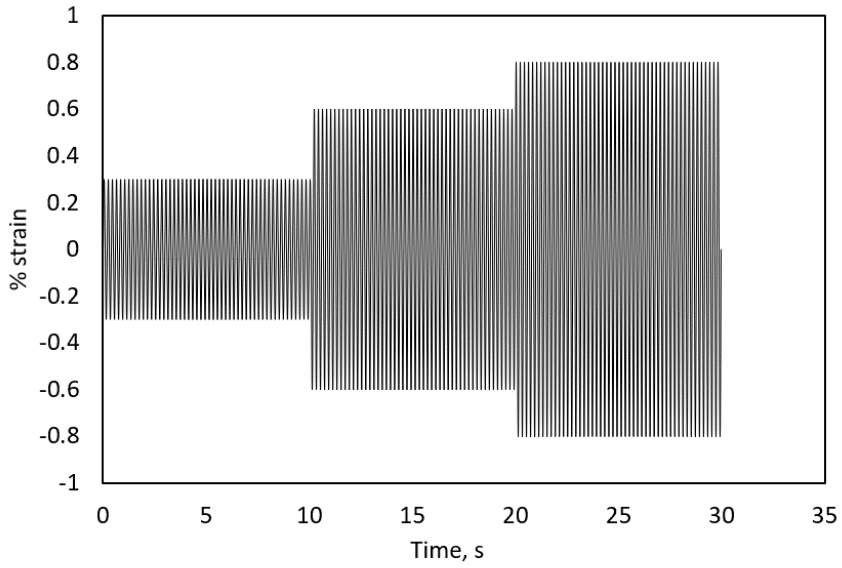

Fig. 4.5. Multi-amplitude strain

Apart from the combined model used in the research, an evolutionary model for the kinematic and isotropic parameters have been employed per equation 2.17. This has shown better accuracy in modelling the cyclic stress-strain behavior. The varying γ_i values predict higher stresses than constant γ_i because the back-stress addition is due to $\frac{C_i}{\gamma_i}$.

Existing finite element tools currently do not incorporate an evolving kinematic hardening model and a USERMAT is required to accurately capture this evolution. An alternative is to define the kinematic parameters using user defined fields utilizing the equation 2.17. Usually, there is provision provided for a single user defined field and that is leveraged here to model the evolving kinematic hardening values. This is cycle by cycle static analysis. The analysis was conducted in three steps, with the amplitude being increased against the cyclic displacement function as shown in figure 4.5. The strain ranges in the multiple amplitude loads were 0.3%, 0.6% and 0.8%.

Material Parameters

The material parameters are directly taken from the work of Pritchard [35]. They are listed in the table below. The given Young's modulus was 173 GPa and the yield strength was at 100.4 MPa.

Table 4.3.
Kinematic hardening parameters for Alloy 617 [35]

Backstresses	C_i **(MPa)**	γ_i
1	1.135e+6	35288
2	1.34e+5	16348
3	1.13e+4	1859.3
4	2500	0

Table 4.4.
Isotropic hardening parameters for Alloy 617 [35]

Q_∞ **MPa**	b
37.61	61.33

Table 4.5.
Kinematic hardening evolution parameters [35]

No.	L_i	d_i
1	-12800	7.496
2	-4875.7	10.07
3	-634.4	18.57
4	0	1

4.2 Simulations of 3D Printed 15-5 PH Stainless Steel

4.2.1 CASE 3: Fatigue Prediction under Constant Amplitude Strain Load: Direct Cyclic Method

The fatigue analysis is carried out using the direct cyclic approach. Stable cycles are reached and, damage initiation and accumulation parameters modify the structure response. The simulation is conducted for three different constant strain amplitude.

Geometry, Mesh and Boundary Condition

The geometry is modeled as standard test specimen for rotating bending fatigue tests presented in Chapter 3. The simple geometry was created using a CAD modeler. The radius of the bending specimen is 4 mm and length is 100 mm per standard specimen. 8 noded Brick elements with reduced integration formulation (C3D8R) are used in this simulation. There are 3792 elements and 4523 nodes. The characteristic length of the elements is 1.58. The elements are created with a bias such that there are

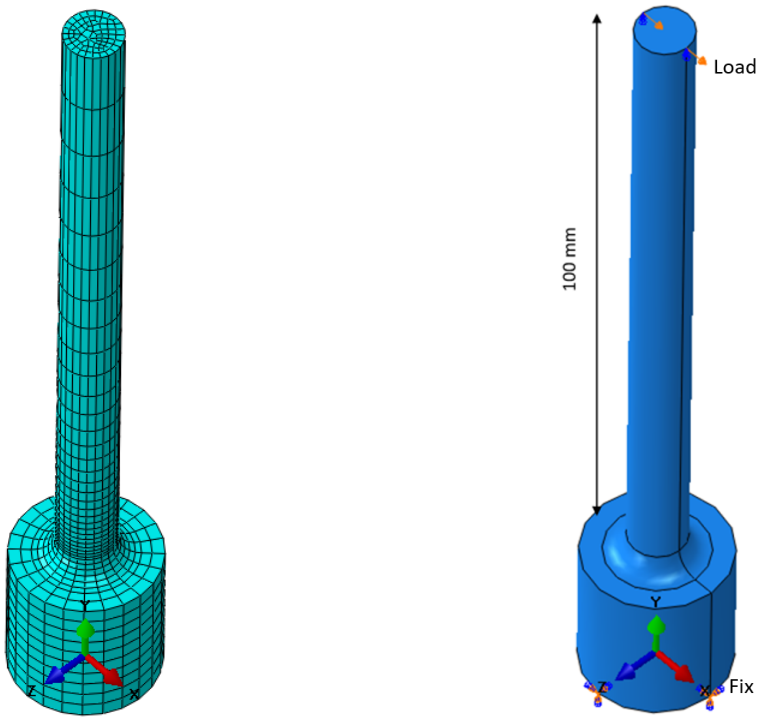

(a) Mesh (b) Boundary condition

Fig. 4.6. FE model for the rotary fatigue specimen

more elements near the fixed point of the cantilever beam as opposed to the free end. The model is constrained at one end and is free to move at the other. A displacement boundary condition is applied to the free end. See figure 4.6(a) and 4.6(b).

The same displacement function shown in 4.2 was used to apply strain loads. The analysis was conducted for three total strain ranges of 1.87%, 1.58% and 1.37%.

Material Parameters

The non-linear hardening models parameters are fit for 4 backstresses from the data of the monotonic stress-strain graph from 4.7. As mentioned before, ideally the fit should be made using both monotonic and cyclic curves. But given the current set of data, we can predict how the material will behave under cyclic loads.

From the stress-strain data it was ascertained that the Young's modulus was 78.85 GPa and yield limit of the specimen was 820 MPa and thus the plastic strain data was captured. The entirety of the data was sampled at an interval of 100 to reduce the data to manageable portion. The C_i and γ_i are listed in the table 4.6, and a curve representing total backstress and it's relation to it's additive components is shown in figure 4.9. The parameter values were obtained by the curve fit (see figure 4.8).

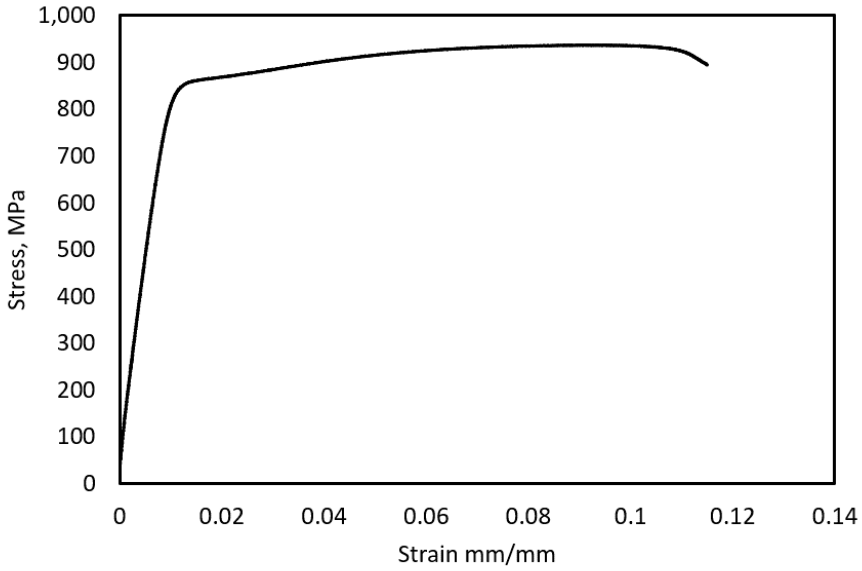

Fig. 4.7. Experimentally measured uniaxial tension Stress-strain graph for 3D printed 15-5 PH stainless steel

Table 4.6.
Backstresses C_i and γ_i values for 3D printed 15-5 PH stainless steel

Backstresses	C_i **(MPa)**	γ_i
1	3.45e+05	23435.577
2	1.44e+05	108732.63
3	2.88e+04	14737.23
4	3.71e+03	37.055

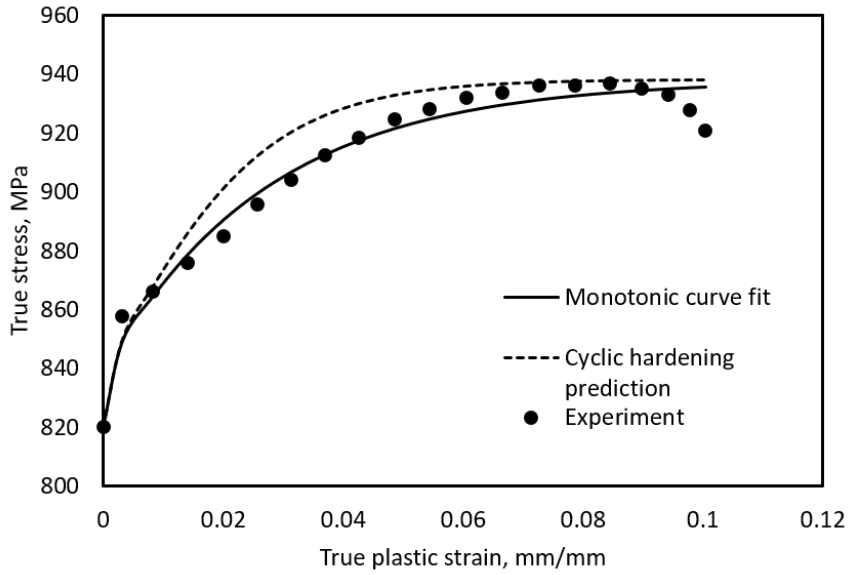

Fig. 4.8. Curve fit applied to experimental data

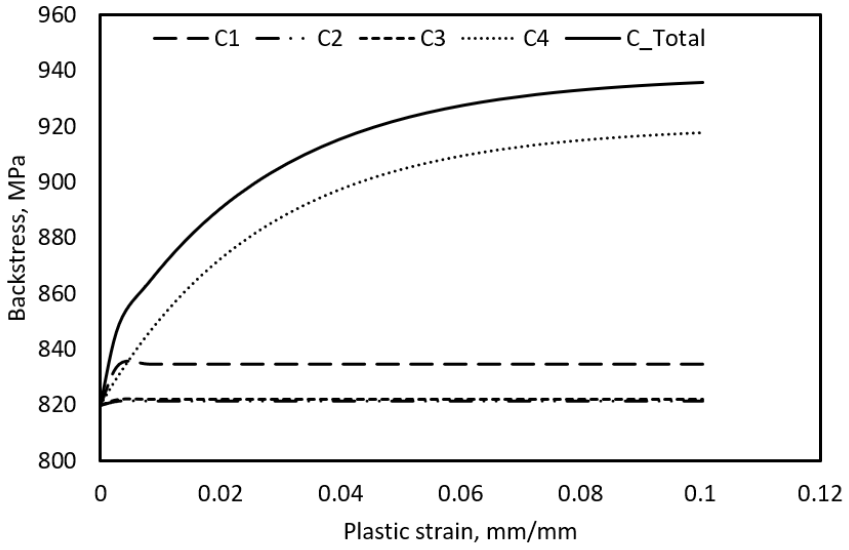

Fig. 4.9. Total backstress(solid line) and it's decomposed components

The damage parameters are calculated to accommodate the values obtained from the experiments. The initiation parameters were taken from Biglari et al. [27] as there is insufficient data to calibrate those parameter. The chosen initiation parameters indicate initiation at a very low hysteresis energy threshold. The damage evolution parameters are calibrated assuming a strain life result and taking the value of mesh dependent characteristic length as 1.58.

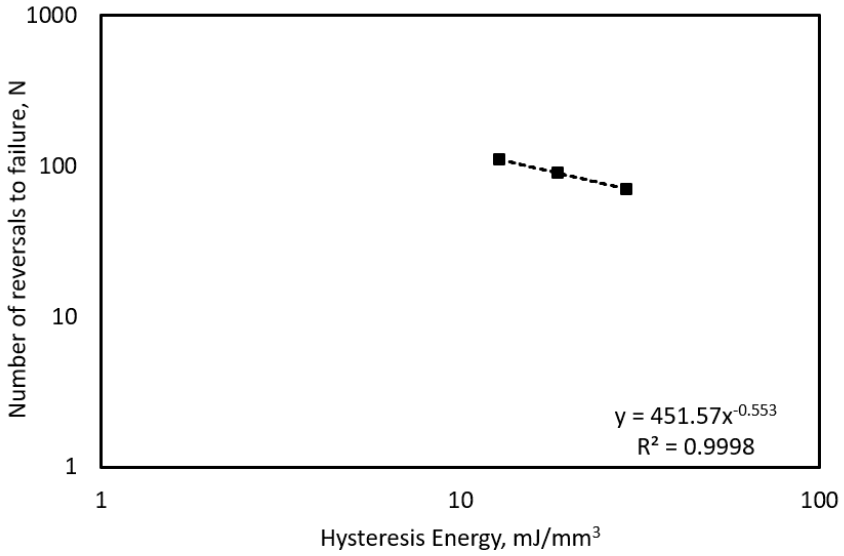

Fig. 4.10. Damage evolution parameter fit

Table 4.7.
Damage parameters for 3D printed 15-5 PH stainless steel

Damage parameters	**Values**
C_1	14.3 [27]
C_2	-0.91 [27]
C_3	1.4e-3
C_4	0.553

4.2.2 CASE 4: Cyclic Behavior Simulation under Multi-amplitude Strain Load: Static Analysis Method

The simulation undertaken in section 4.1.2 is repeated for the case of 15-5 PH stainless steel. The axisymmetric geometry, mesh and boundary condition is similar to the ones used in the mentioned section. The Young's modulus and yield strength for 15-5 PH stainless steel from the stress-strain data is used (see section 4.2) and kinematic hardening material property used is the same as in table 4.6. In this case, the kinematic hardening evolution parameters are included.

The kinematic hardening evolution parameters are take from the reference used in section 4.1.2 in table 4.5 [6]. The procedure remains similar to section 4.1.2. Only the displacement amplitudes are changed for this simulation as seen in figure 4.11. The displacement amplitudes are different because, 15-5 PH stainless steel yields at a much higher strain than Alloy 617 used in section 4.1.2.The multi-amplitude strain range has the split 1.15%, 1.6% and 1.75%.

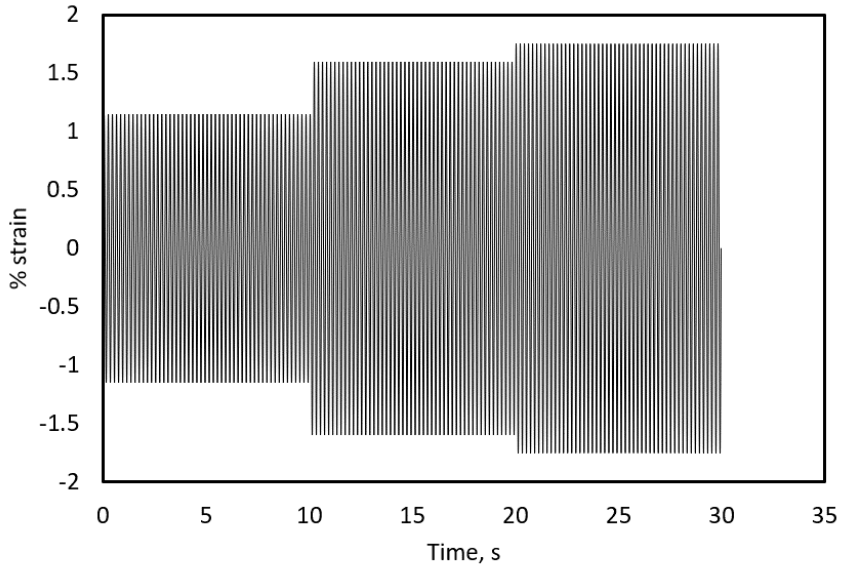

Fig. 4.11. Multi-amplitude strain for CASE 4

4.3 Results and Discussion

4.3.1 CASE 1: Fatigue Prediction for 3D Printed 17-4 Stainless Steel under Constant Amplitude Strain Load

Since, the calibration was done using the cyclic test data, the cyclic response of the material should be compared with the literature. Cyclic stress-strain response for several strain amplitude ranges are captured. As seen in figure 4.12, the hardening regions of respective cycles from the results of FEA closely match the experimental cyclic stress-strain curve [6]. The material shows cyclic hardening ability and it is correctly predicted in the current model. The evolution of damage can be seen

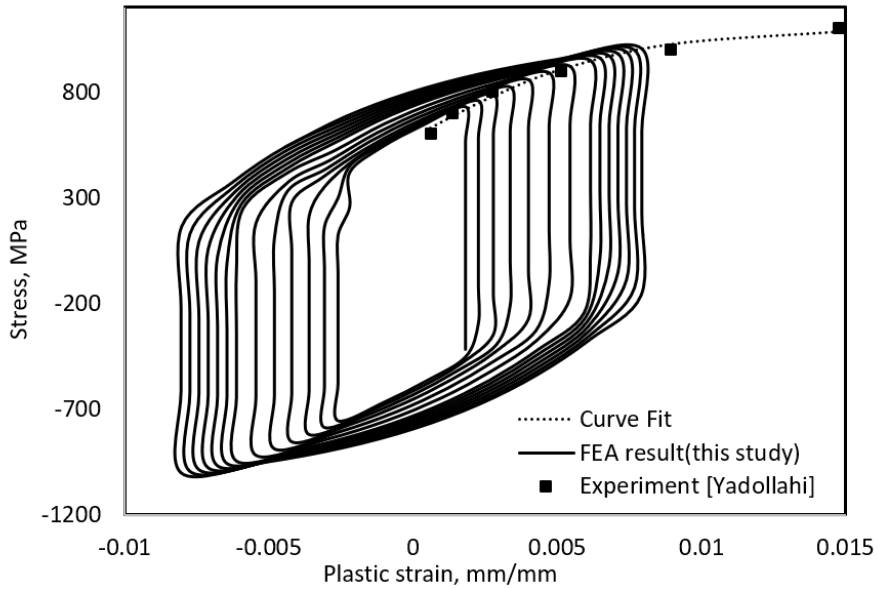

Fig. 4.12. Family of cyclic stress-strain curves for different strain ranges

in the normalized damage vs Cycles graph shown in figure 4.13. As is expected, the specimen damages quickly when loaded at a higher strain range as compared with low strain range. For the damage initiation criteria prescribed, only specimen subjected to 0.3% strain showed delayed initiation, at 971 cycles (seen as flat curve before damage $D > 0$). The strain-life curve obtained is shown in figure 4.14. It shows

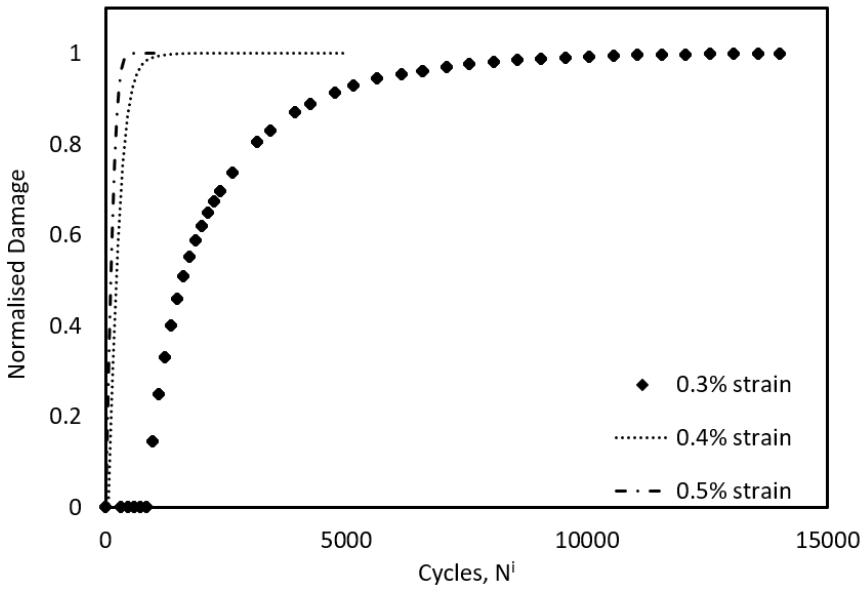

Fig. 4.13. Normalised damage vs cycles

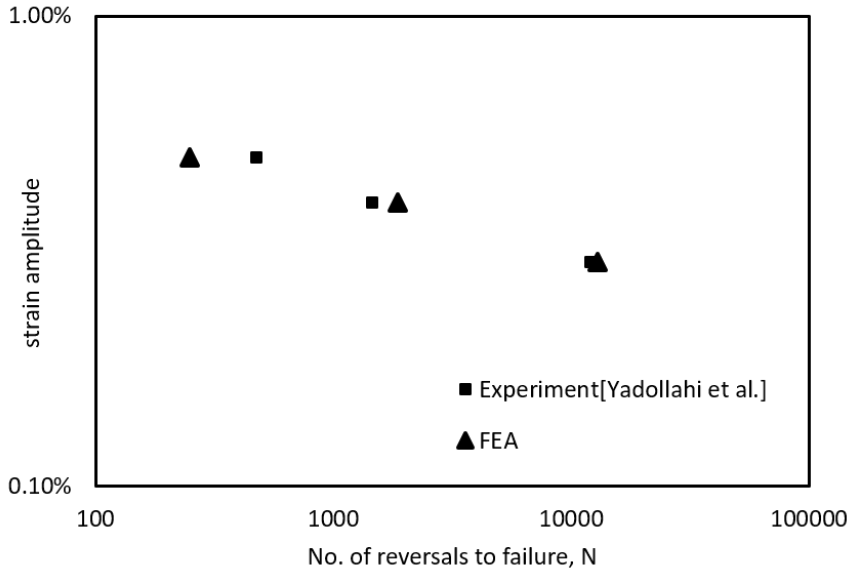

Fig. 4.14. Strain life curve for vertically printed as built 17-4 stainless steel

reasonable agreement with experimental results from literature [6]. The accuracy of the prediction depends on correct fit using large number of data points. The present model is limited as the calibration data was insufficient.

4.3.2 CASE 2: Cyclic Behavior Simulation for Alloy 617 under Multi-amplitude Strain Load

The modified parameters were a reasonable approximation as it captured the intended effect on stress evolution. As discussed earlier, the introduction of the kinematic hardening evolution parameter ensures that higher stresses are predicted for the same plastic strain regime since the given values of L_i and d_i cause the γ_i value to decrease, which in turn causes the backstress values to increase. Figure 4.15 shows this comparison of the results obtained using modified parameters in FEA and the results from literature.

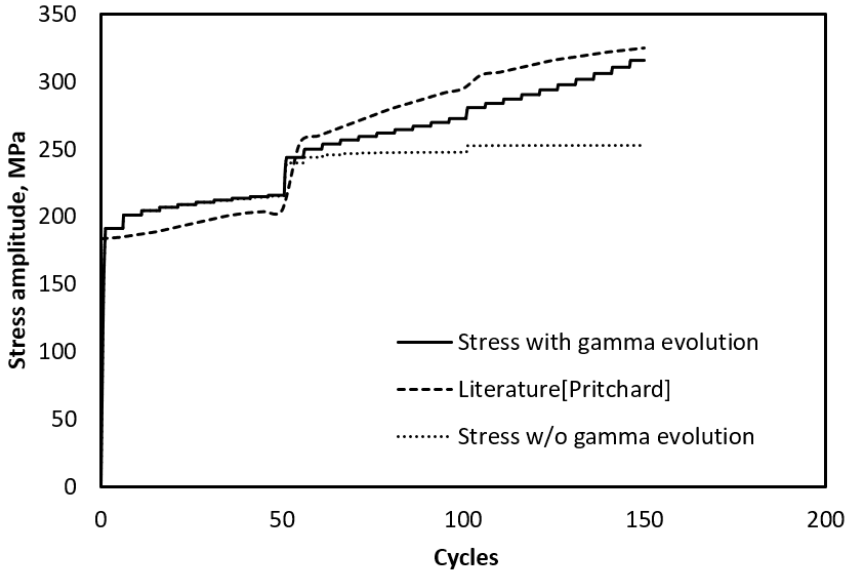

Fig. 4.15. Comparison of FEA result with literature [35]

The variation of the stress-strain curves are shown for different cycles in the figure 4.16. This figures captures the effect of combined hardening model used. We can see that the hysteresis loops shift upwards for higher cycles within a strain range. The kinematic evolution parameters indicate an increased number of cycles to a stabilized regime. As, the load is increased, the material would resist hardening (stress response will plateau) and damage would initiate. After this, the material would soften..

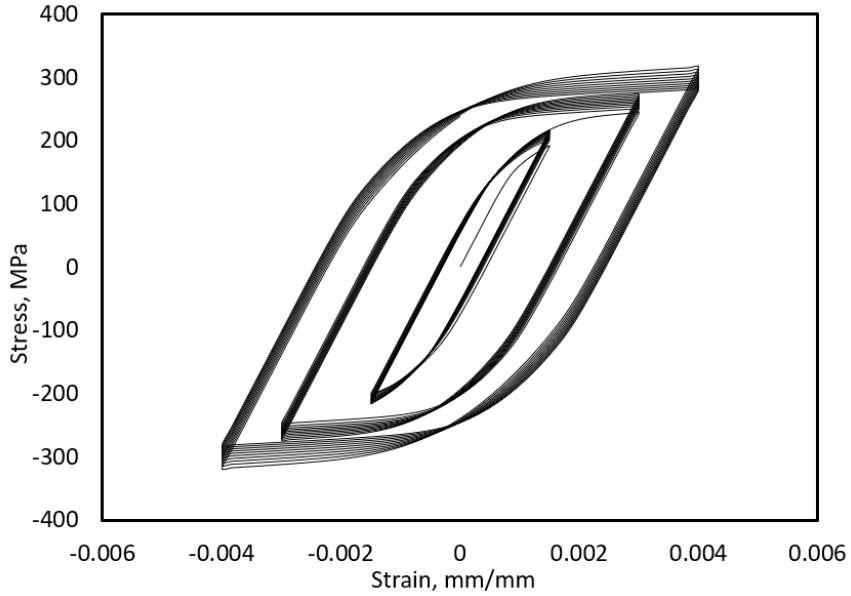

Fig. 4.16. Variation of stress-strain loops for different strain range

4.3.3 CASE 3: Fatigue Prediction for 3D printed 15-5 PH Stainless Steel under Constant Amplitude Strain Load

The progression of damage parameter as cycles progress for different strain ranges are shown in figure 4.17. Since the damage initiation parameters are nominal, damage would begin for minimal hysteresis energy, which is achieved at all strain amplitude ranges in our simulations.

The rate of energy dissipation, and thus that of damage evolution, would be highest for the highest strain amplitude range and this is seen in the figure. The damage parameter has a power law relationship with cycles and thus is non-linear. The calibration of damage evolution of damage parameters shows good agreement with values used to calibrate (see figure 4.18). The predicted strain life from finite element model and the calibration life values are close to each other with higher strains resulting in shorter life. The results would be more accurate with large data points as it would smooth-en the curve out.

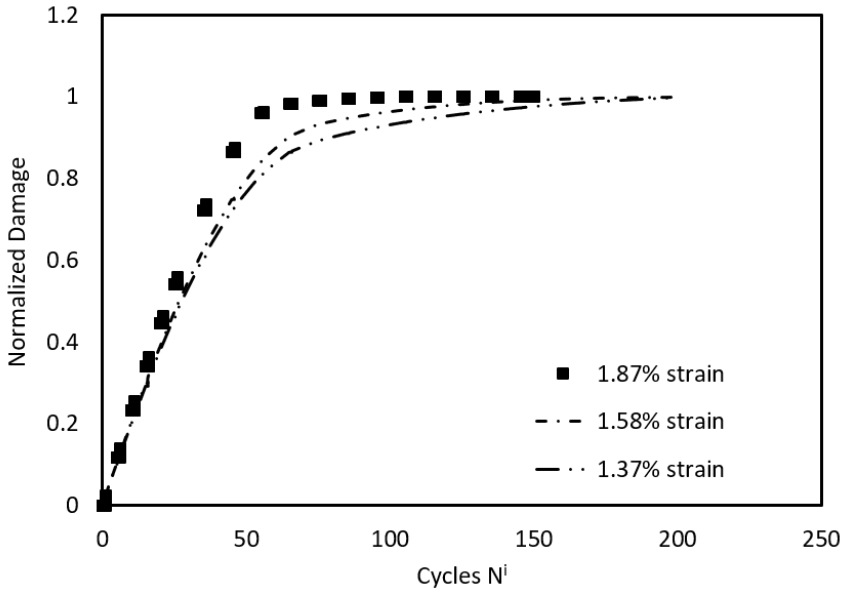

Fig. 4.17. Variation of damage parameter with cycles for different strain ranges

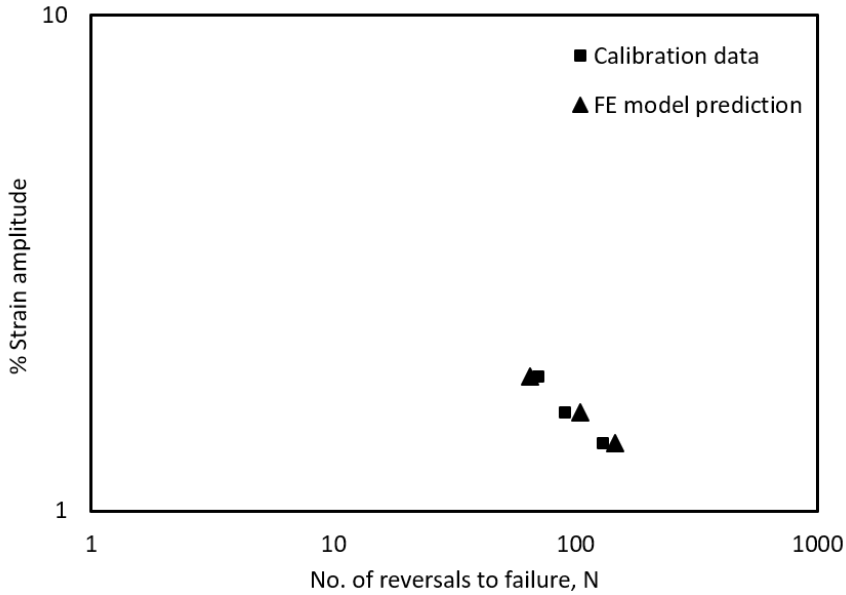

Fig. 4.18. Comparison of strain life curve between fit data and FEA

The model is extended (see figure 4.19) to cover the lower strain regions that the experiment covered. The Coffin-Manson-Basquin combined law is fit and the predicted curve passes close to the experimental values. The Coffin-Manson-Basquin parameters referring equation 2.4 is given in table 4.8.

Table 4.8.
Coffin-Mason-Basquin parameters for 3D printed 15-5 PH stainless steel

Parameters	**Values**
$\sigma_f^{'}\ GPa$	70.92
b	-0.7455
$\epsilon_f^{'}$	9.884
c	-0.405

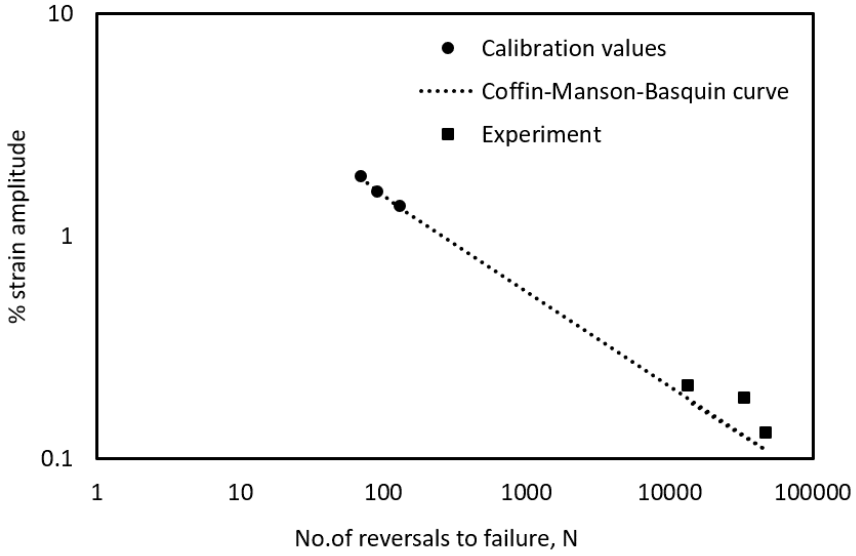

Fig. 4.19. Comparison between experimental data and Coffin-Manson-Basquin prediction for 3D printed 15-5 PH stainless steel

The variation of stress for the strain amplitude loading of 1.87% can be seen from figure 4.20. As, in our simulation, damage starts at the first cycle, the material softens

as it is loaded through cycles. If we compare the von-Mises stress values at the point of maximum amplitude during each of the cycles, we see that the overall maximum von-Mises stress values are decreasing (see figures 4.20(a), 4.20(b) and 4.20(c)) from 869 MPa at cycle 1 to 842 MPa at cycle 65 near failure.

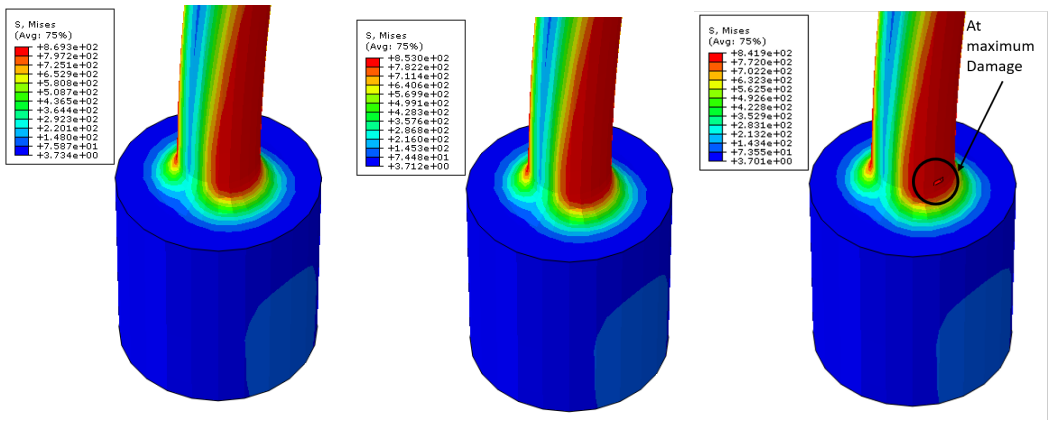

(a) Cycle 1 (b) Cycle 35 (c) Cycle 65

Fig. 4.20. Von Mises stress plots for the model at different cycles with damaged material at 65th cycle

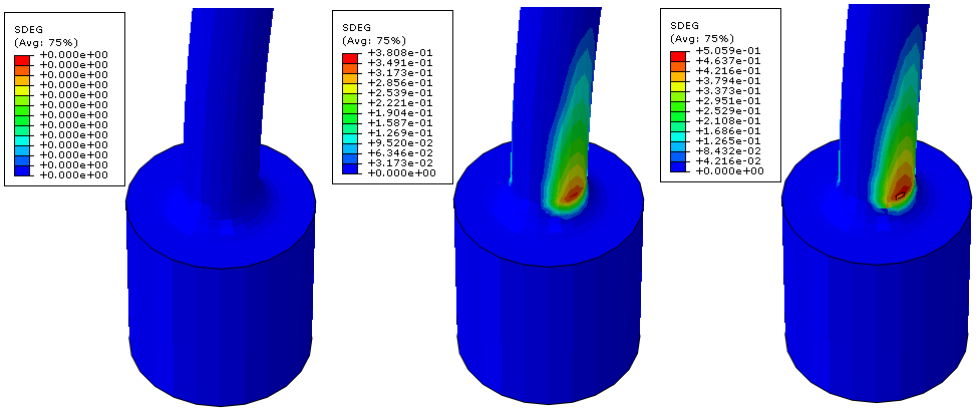

(a) Cycle 1 (b) Cycle 35 (c) Cycle 65

Fig. 4.21. Damage parameter at different cycles with damaged material at 65th cycle

The corresponding damage parameter plot at different cycles are plotted in figure 4.21. On the first cycle we see that the damage has not initiated yet, because, as per our criterion, damage initiation is after the first cycle. The damage progresses as the specimen is cycled through constant amplitude strain and reaches it's maximum value at cycle 65 for failure. At this stage, the material has lost it's capacity for plastic work.

4.3.4 CASE 4: Cyclic Behavior Simulation for 3D Printed 15-5 PH Stainless Steel under Multi-amplitude Strain Load

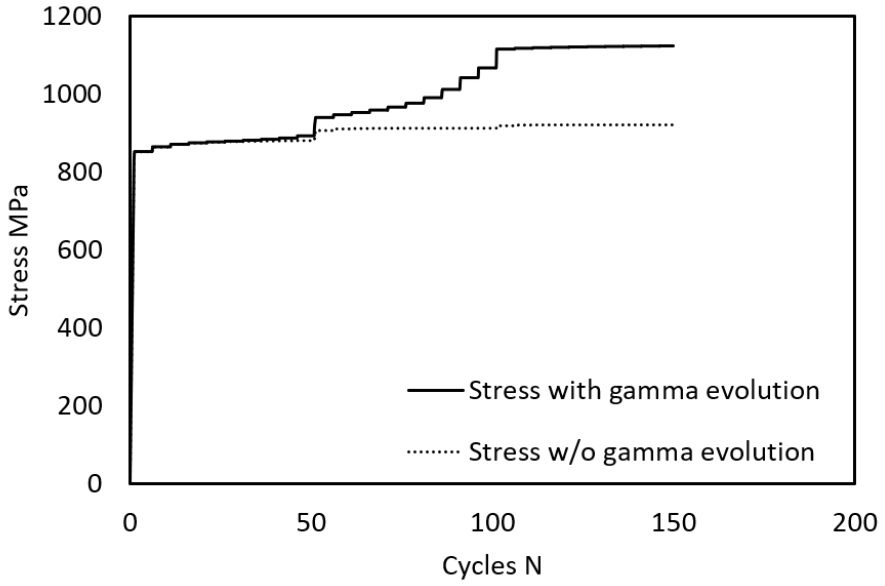

Fig. 4.22. Cycle dependent stress variation

The kinematic hardening evolution parameters used in this model increased the backstress component during stress-strain reversals. As is seen in figure 4.22 the predicted values of stresses are higher when hardening evolution model is used. Since, these values are borrowed from literature, the actual stress evolution behavior needs to be tracked and then the γ_i evolution needs to be calibrated to new L_i and d_i values to accurately capture the behavior.

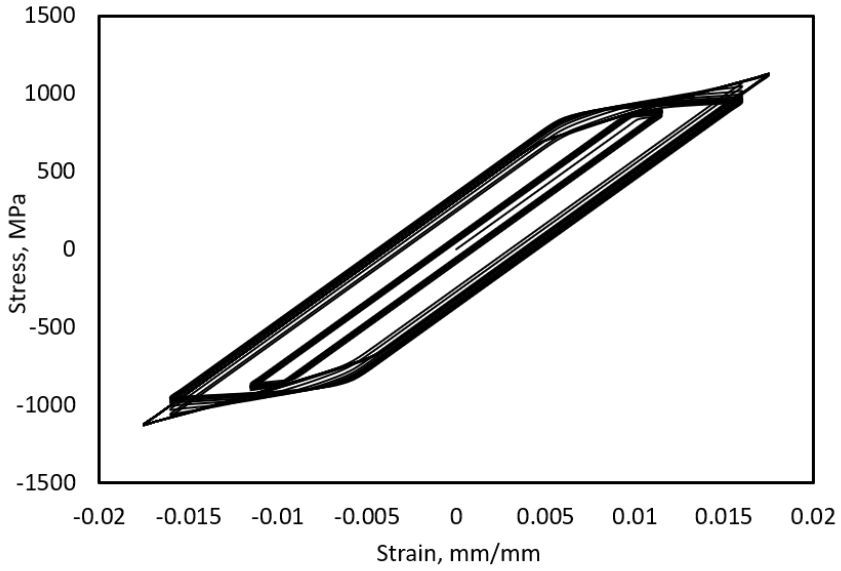

Fig. 4.23. Stress-strain curve

The stress-strain graph is shown in figure 4.23 associated with the hardening evolution model. The yield limit of 15-5 PH stainless steel is several times higher than the values used for Alloy 617 and the hysteresis curve would be narrower. This could indicate a more brittle interaction as compared to Alloy 617.

5. CONCLUSION

In this thesis, a combined numerical and experimental study is presented. The major conclusions are summarized as follows.

- The fatigue life of the 15-5 PH stainless steel is experimentally measured. The strain life curve shows that the numbers of the reversals to failure increase from 13,403 to 46,760 as the applied strain magnitudes decrease from 0.214% from 0.132%, respectively. The microstructure analysis shows that predominantly brittle fracture is presented on the fractured surface

- A finite element model based on cyclic plasticity including the damage model is developed to predict the fatigue life. The model is calibrated with two cases: one is the fatigue life of 3D printed 17-4 stainless steel under constant amplitude strain load using the direct cyclic method, and the other one is the cyclic behavior of Alloy 617 under multi-amplitude strain loads using the static analysis method. Both validation models show a good correlation with the literature experimental data

- After the validation, the finite element model is applied to the 15-5 PH stainless steel. Using the direct cyclic method, the model predicts the fatigue life of 15-5 PH stainless steel under constant amplitude strain. The extension of the prediction curve matches well with the previously measured experimental results, following the Coffin-Manson-Basquin Law. Under multi-amplitude strain, the kinematic hardening evolution parameter is incorporated into the model. Higher stresses are predicted when strain amplitudes are increased

- The model presented in the work can be used to design for the reliability of 3D printed metals under cyclic loading conditions.

6. RECOMMENDATIONS

The current model can be further implemented as follows,

- Conduct fatigue tests at low-cycle conditions to better compare against modeling data.
- The strain controlled cyclic tests need to be conducted for 15-5 PH stainless steel to find the cycles to stabilization, cycles to damage initiation and the rate of decrease of the materials ability to do plastic work. This would help characterize the material behavior with greater accuracy.
- These cyclic tests should be conducted for different strain rates and an understanding of strain rate dependence on the fatigue life needs to be assessed.
- The cyclic tests can also incorporate temperature dependency and understand the effects on cyclic behavior.
- For components produced by different 3D printing process, the relationship between 3D printing parameters and the parameters in the model need to be determined.
- This model should be used to predict the fatigue life for different design parameters under complex loading conditions. This knowledge can then guide the design intent.
- The model can be extended to incorporate the effect of creep.

REFERENCES

REFERENCES

[1] P. Paris, M. Gomez, and W. Anderson, "A rational analytical theory of fatigue the trend in engineering," *U. of Washington, Seattle, Wa*, vol. 13, no. 1, 1961.

[2] J. Sehrt and G. Witt, "Dynamic strength and fracture toughness analysis of beam melted parts," in *Proceedings of the 36th international MATADOR conference*. Springer, 2010, pp. 385–388.

[3] A. B. Spierings and G. Levy, "Comparison of density of stainless steel 316l parts produced with selective laser melting using different powder grades," in *Proceedings of the Annual International Solid Freeform Fabrication Symposium*. Austin, TX, 2009, pp. 342–353.

[4] T. L. Starr and A. Spierings, "Tensile and fatigue performance of laser sintered stainless steels," in *Proceedings of the Annual International Solid Freeform Fabrication Symposium, Austin, Texas*. HW-Verlag, 2010.

[5] A. B. Spierings, N. Herres, and G. Levy, "Influence of the particle size distribution on surface quality and mechanical properties in am steel parts," *Rapid Prototyping Journal*, vol. 17, no. 3, pp. 195–202, 2011.

[6] A. Yadollahi, N. Shamsaei, S. M. Thompson, A. Elwany, and L. Bian, "Effects of building orientation and heat treatment on fatigue behavior of selective laser melted 17-4 ph stainless steel," *International Journal of Fatigue*, vol. 94, pp. 218–235, 2017.

[7] R. Branco, J. Costa, F. Berto, S. Razavi, J. Ferreira, C. Capela, L. Santos, and F. Antunes, "Low-cycle fatigue behaviour of aisi 18ni300 maraging steel produced by selective laser melting," *Metals*, vol. 8, no. 1, p. 32, 2018.

[8] L. Tóth and S. Y. Yarema, "Formation of the science of fatigue of metals. part 1. 1825–1870," *Materials Science*, vol. 42, no. 5, pp. 673–680, 2006.

[9] R. Smith, "The versailles railway accident of 1842 and the first research into metal fatigue.(retroactive coverage)," *Fatigue 90*, pp. 2033–2041, 1990.

[10] O. Basquin, "The exponential law of endurance tests," in *Proc Am Soc Test Mater*, vol. 10, 1910, pp. 625–630.

[11] A. Milton, "Miner: Cumulative damage in fatigue journal of appl," *Mech*, 1945.

[12] L. Coffin, "The cyclic straining and fatigue of metals," *Trans Metall Soc AIME*, vol. 215, p. 794, 1959.

[13] S. Manson and M. Hirschberg, "Fatigue: an interdisciplinary approach," *Syracuse University Press, Syracuse, NY*, p. 133, 1964.

[14] S. Manson, "Fatigue: a complex subjectsome simple approximations," *Experimental mechanics*, vol. 5, no. 7, pp. 193–226, 1965.

[15] W. Cui, "A state-of-the-art review on fatigue life prediction methods for metal structures," *Journal of marine science and technology*, vol. 7, no. 1, pp. 43–56, 2002.

[16] W. R. Osgood, "Stress-strain formulas," *Journal of the Aeronautical Sciences*, vol. 13, no. 1, pp. 45–48, 1946.

[17] R. Hill, *The mathematical theory of plasticity*. Oxford university press, 1998, vol. 11.

[18] J.-L. Chaboche, "A review of some plasticity and viscoplasticity constitutive theories," *International journal of plasticity*, vol. 24, no. 10, pp. 1642–1693, 2008.

[19] J. Bauschinger, "On the changes of the elastic limit and the strength of iron and steel by straining in tension and compression, by heating and by cooling and by frequently repeated loading," *Mitt Mech*, vol. 13, no. 3, pp. 1–115, 1886.

[20] J. Bree, "Elastic-plastic behaviour of thin tubes subjected to internal pressure and intermittent high-heat fluxes with application to fast-nuclear-reactor fuel elements," *Journal of strain analysis*, vol. 2, no. 3, pp. 226–238, 1967.

[21] C. O. Frederick and P. Armstrong, "A mathematical representation of the multiaxial bauschinger effect," *Materials at High Temperatures*, vol. 24, no. 1, pp. 1–26, 2007.

[22] S. Krishna, T. Hassan, I. B. Naceur, K. Saï, and G. Cailletaud, "Macro versus micro-scale constitutive models in simulating proportional and nonproportional cyclic and ratcheting responses of stainless steel 304," *International Journal of Plasticity*, vol. 25, no. 10, pp. 1910–1949, 2009.

[23] J. Lemaitre, *A Course on Damage Mechanics*, 2nd ed. Springer Science Business Media, 1996.

[24] L. Kachanov, *Introduction to continuum damage mechanics*. Springer Science & Business Media, 2013, vol. 10.

[25] Y. N. Rabotnov, *Creep problems in structural members*. North-Holland Series in Applied Mathematics and Mechanics, 1969, vol. 7.

[26] D. Dewees, "Ratcheting and cyclic plasticity considerations for code analysis," (Retrieved 06-May-2019). [Online]. Available: https://www.efatigue.com/training/Chapter_5.pdf

[27] F. Biglari, P. Lombardi, S. Budano, C. Davies, and K. Nikbin, "Predicting damage and failure under low cycle fatigue in a 9cr steel," *Fatigue & Fracture of Engineering Materials & Structures*, vol. 35, no. 12, pp. 1079–1087, 2012.

[28] K. D. Van and M. H. Maitournam, "On a new methodology for quantitative modeling of fretting fatigue," in *Fretting fatigue: current technology and practices*. ASTM International, 2000.

[29] "Abaqus user manual V6.14," (Retrieved 01-May-2019). [Online]. Available: https://abaqus-docs.mit.edu/2017/English/SIMACAETHERefMap/simathe-c-directcyclic.htm

[30] Z. P. Bažant and J. Ožbolt, "Nonlocal microplane model for fracture, damage, and size effect in structures," *Journal of Engineering Mechanics*, vol. 116, no. 11, pp. 2485–2505, 1990.

[31] "Abaqus user manual V6.14," (Retrieved 01-May-2019). [Online]. Available: https://abaqus-docs.mit.edu/2017/English/SIMACAEANLRefMap/simaanl-c-directcyclicfatigue.htm

[32] "EOS stainless steel PH1 for EOSINT M 270," (Retrieved 06-March-2018). [Online]. Available: http://gpiprototype.com/images/PDF/EOS-StainlessSteel-PH1.pdf

[33] "TERCO MT3012 fatigue tester," (Retrieved 06-May-2018). [Online]. Available: https://www.tercosweden.com/wp-content/uploads/2019/04/Material-Testing-Lab_Lres.pdf

[34] S. Sagar, Y. Zhang, L. Wu, H.-Y. Park, J.-H. Lee, Y.-G. Jung, and J. Zhang, "Room-temperature charpy impact property of 3d-printed 15-5 stainless steel," *Journal of Materials Engineering and Performance*, vol. 27, no. 1, pp. 52–56, 2018.

[35] P. G. Pritchard, "High temperature fatigue and fatigue-creep responses of alloy 617-experimental and unified constitutive modeling." Master's thesis, North Carolina State University, 2014.

VITA

VITA

List of Publications

Padmanabhan, A., & Zhang, J. (2018). Cybersecurity risks and mitigation strategies in additive manufacturing. Progress in Additive Manufacturing, 3(1-2), 87-93.

List of Presentations

Padmanabhan, A., & Zhang, J.(2018, April). *Fatigue characterization of 3D printed 15-5 stainless steel*. Poster session presented at IUPUI Research Day, Indianapolis, Indiana.

Padmanabhan, A., Sagar, S. & Zhang, J.(2018, June). *Temperature-dependent Impact Properties of 3D Printed 15-5 Stainless Steel* . Poster session presented at POWDERMET2018 conference, San Antonio, Texas.

Padmanabhan, A., & Zhang, J.(2018, June). *Fatigue characterization of 3D printed 15-5 stainless steel*. Poster session presented at POWDERMET2018 conference, San Antonio, Texas.

Padmanabhan, A., & Zhang, J.(2018, October). *Analysis of fatigue behavior of 3D printed 15-5 stainless steel - A combined modeling and experimental approach*. Paper presented at MS&T conference, Columbus, Ohio.

Awards

National science foundation(NSF) travel grant for POWDERMET2018.